Study of a Jet Pipe Electropneumatic Actuator

by

Paul D. Henri
Department of Biomedical Engineering
McGill University, Montreal

A THESIS SUBMITTED TO THE FACULTY OF GRADUATE
STUDIES AND RESEARCH IN PARTIAL FULFILLMENT OF
THE REQUIREMENTS FOR THE DEGREE OF
MASTER OF ENGINEERING

April, 1994

Abstract

This thesis presents the results of an investigation of a jet pipe electropneumatic actuator designed for use in the Utah/MIT Dextrous Hand (UMDH). A survey of dextrous hand systems and their related technologies is also provided.

As part of an effort to characterize the UMDH system as a whole, a nonlinear mathematical model of the actuator is given including detailed representation of the jet pipe element, orifice areas and fluid dynamics. Model parameters are identified and the model formulation is validated through experimentation and simulation.

The performance of the actuator under closed-loop control is examined. Experimental results show that feedforward control is useful in eliminating any steady-state offset and that a stable bandwidth of 80 Hz is achievable using a simple proportional feedback controller. A linearized model of the actuator is presented and compared with the nonlinear model. Results show that linearized model adequately describes the actuator dynamics at the specified operating point.

The agreement between simulations and experimental data indicates that the mathematical models presented are potentially valuable tools, whether to aid in the analysis and design of actuation systems, or for use in model-based control.

Résumé

Cette thèse présente les résultats de l'étude d'un actuateur électropneumatique à "jet pipe", spécialement conçu pour être utilisé avec la Main Habile Utah/MIT. Un aperçu des systèmes à main habile est présenté, ainsi que les technologies qui leur sont reliées.

S'insérant dans l'effort de caractériser la main dans son ensemble, un modèle mathématique non-linéaire de l'actuateur est fourni. Ce modèle inclue une représentation détaillée de l'élément "jet pipe", des aires d'orifices et de la dynamique des fluides. Les paramètres du modèle sont identifiés et la formulation du modèle est validée par le biais de simulations et d'expériences.

La performance de l'actuateur sous contrôle boucle-fermée est étudiée. Les résultats expérimentaux démontrent que le contrôle à pré-alimentation est utile pour éliminer toute constante d'erreur en régime permanent. Ils démontrent aussi qu'il est possible d'obtenir une bande de fréquence stable de 80 Hz en utilisant un simple contrôleur proportionel à rétro-action. Un modèle linéarisé de l'actuateur est presenté, puis comparé avec le modèle non-linéaire. Les résultats démontrent que le modèle linearisé décrit adéquatement la dynamique de l'actuateur.

L'accord entre les données expérimentales et celles obtenues par simulation indique que les modèles mathématiques présentés sont des outils potentiellement valables, que ce soit pour l'analyse et la conception de systèmes d'actuation, ou pour l'usage d'un contrôle basé sur un modèle.

Acknowledgements

I wish to thank Professor John Hollerbach for his guidance throughout this work. His patience, understanding and expertise is inspiring and sincerely appreciated.

I also wish to thank my colleagues and friends. Dr. Yangming Xu and Robert Rohling for their technical assistance and many helpful insights. They were always a source of lively discussions and fresh ideas, whether I felt I needed them or not.

The resources of Professor Ian Hunter are also gratefully acknowledged, as is the first-class machining assistance provided by Sander Boelen.

Finally, I thank my family for their faith and support, and for believing in me. In closing, I wish to dedicate this thesis to the memory of my father, Norman Leslie Henri.

List of Figures

List of Tables

Nomenclature

A_{jp}	jet pipe exit area [m^2]
A_{lpp}	leakage-past-piston area [m^2]
A_p	piston area [m^2]
A_{r1}, A_{r2}	orifice return areas [m^2]
A_{s1}, A_{s2}	orifice supply areas [m^2]
C_d	orifice discharge coefficient [non-dim]
$C_{d,lpp}$	leakage-past-piston discharge coefficient [non-dim]
C_{db}	leakage-past-piston discharge coefficient offset [non-dim]
C_{dm}	leakage-past-piston discharge coefficient slope [non-dim]
D	diameter [m]
D_{cyl}	inside diameter of cylinder [m]
D_{jp}	inside diameter of jet pipe [m]
F_{act}	actuator force [N]
F_a	actual actuator force [N]
F_c	Coulomb friction force on piston [N]
F_d	desired actuator force [N]
F_f	dry friction force on piston [N]
F_{jp}	jet pipe tip force [N]
F_{spring}	spring force [N]
i	current [A]
$\bar{i}$	static current [A]
i_{offset}	current driver offset [A]
k_{cd}	current driver gain [A/V]
k_m	motor torque constant [N/A]

k_p	feedback position gain [A/N]
k_{spring}	spring constant [N/m]
L_{cyl}	length of cylinder [m]
L_p	length of piston [m]
L_s	length of stopper [m]
L_{spring}	length of spring (loaded) [m]
$L_{spring,0}$	length of spring (unloaded) [m]
L_{sup}	length of support [m]
$\dot{m}_i$	net mass flow rate for chamber i [kg/s]
$\dot{m}_{lpp}$	mass flow rate past piston [kg/s]
m_p	mass of piston [kg]
$\dot{m}_{r1}$, $\dot{m}_{r2}$	return mass flow rates for chambers 1 and 2 [kg/s]
$\dot{m}_{s1}$, $\dot{m}_{s2}$	supply mass flow rates for chambers 1 and 2 [kg/s]
P_{atm}	atmospheric pressure [Pa]
P_i	pressure in chamber i [Pa]
$\dot{P}_i$	rate of change of pressure for chamber i [Pa/s]
P_s, P_r	supply and return pressures [Pa]
P_u, P_d	upstream and downstream pressures [Pa]
Q_i	volumetric flow rate for chamber i [m^3/s]
R	gas constant [j/kg·K], also radius [m], also resistance [Ω]
r_c	critical pressure ratio [non-dim]
t	time [s]
T_i	temperature for chamber i [K]
T_s, T_r	supply and return temperatures [K]
T_u, T_d	upstream and downstream temperatures [K]
$v_{D/A}$	D/A voltage [V]
V_i	volume of chamber i [m^3]
$\dot{V}_i$	rate of change of volume for chamber i [m^3/s]

x_{jp}	jet pipe position (relative) [m]
$\bar{x}_{jp}$	static jet pipe position (relative) [m]
$x_{jp,abs}$	jet pipe position (absolute) [m]
$x_{jp,offset}$	jet pipe offset [m]
x_p	piston position [m]
x_s	stopper position [m]
γ	isentropic exponent [non-dim]
ρ_i	density of air in chamber i [kg/m^3]
ω_1, ω_2	jet pipe corner frequencies [rad/s]
ω_{cd}	current driver corner frequency [rad/s]
ω_{cl}	closed-loop actuator bandwidth [rad/s]
ζ_2	jet pipe damping ratio [non-dim]

1. Introduction

In recent years, much effort has been devoted to the design, construction and control of articulated, multifingered robotic hands. The development and use of dextrous hands is an enormously complicated affair involving the close integration of many sub-areas of research including mechanism design, actuation system design, control theory, tactile sensing, grasp planning, kinematic calibration and telemanipulation. Careful study of the individual components that comprise such advanced systems is required if one is to gain a better understanding of the nature of machine dexterity (Jacobsen et al. [1984b]).

This thesis reports on the study of the actuation system of the Utah/MIT Dextrous Hand (UMDH) and presents an experimentally verified mathematical model for one of the system's pneumatic actuators. This project represents the first step in characterizing the robot hand system as a whole and is fundamental to the goal of improved control.

An overview of dextrous hand systems is presented in the following section, which describes the features of a variety of dextrous hands with an emphasis on their actuation systems.

1.1 Dextrous Robot Hands

A number of dextrous robot hands have been constructed for use as research tools with three being made commercially available (Utah/MIT Dextrous Hand, Stanford/JPL Dextrous Hand and Belgrade/USC Dextrous Hand). These hands vary widely in their designs, sensor array and actuation systems. Some of these hands are anthropomorphic while others are not. Narasimhan [1988] presents a history of dextrous hand development along with kinematic and control issues. Figure 1.1 itemizes

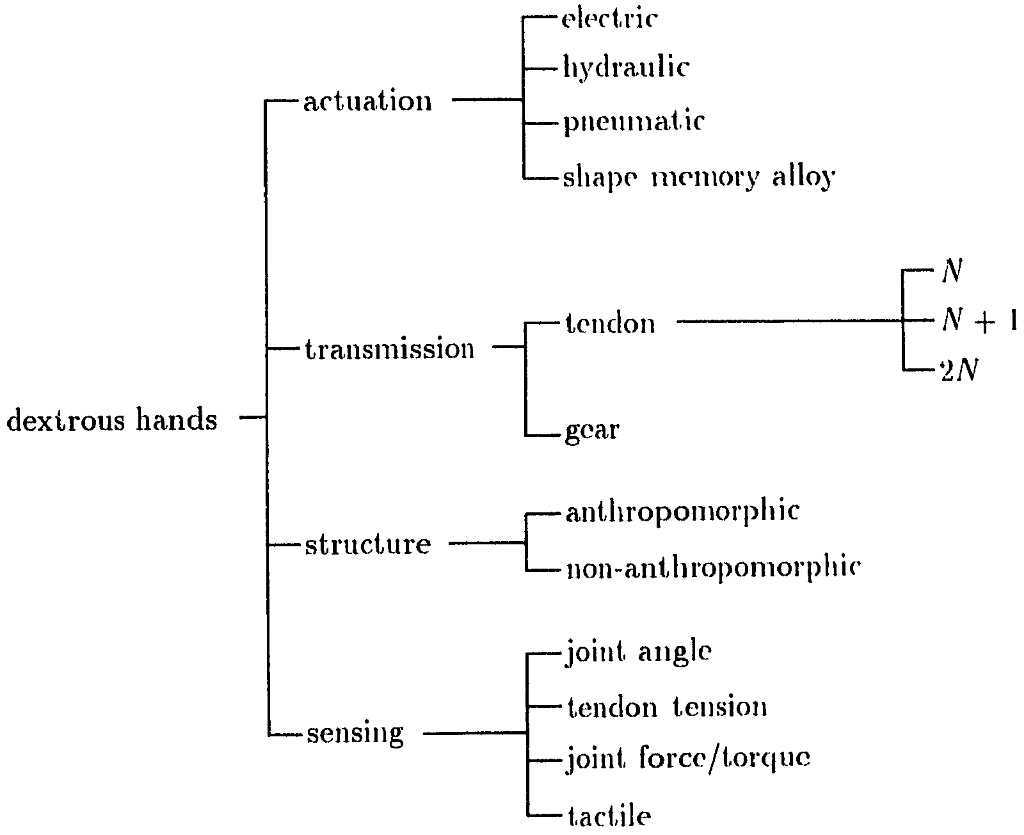

Figure 1.1: Physical features of dextrous hand systems.

the main physical features of dextrous hand systems.

The choice of actuator type has traditionally been DC rotary motors, although several hands have used linear pneumatic or Nickel-Titanium (NiTi) shape memory alloy (SMA) actuators. In general, the choice of actuator type depends on power/mass, force/mass, bandwidth, stroke and size factors. Hollerbach et al. [1992] provide a comparative analysis of actuator technologies for robotics. A short description of typical actuation systems used for dextrous hands in given in §1.3.

Most dextrous hand designs feature tendon or belt transmission systems. The advantages of such drive systems are numerous (Townsend and Salisbury [1988]) and include such factors as low inertia and flexible transmission paths. However, the most

Hand or Reference	Fingers	Joints	Actuation	Transmission	Config.
Anthrobot-2	5	20	DC motor	tendon-pulley	N
Belgrade/USC	5	15	DC motor	tendon-pulley	—
Hitachi[a]	3	12	SMA	tendon-sheath	N
JPL[b]	4	16	DC motor	tendon-pulley	N
Kuribayashi [1986]	3	9	SMA	tendon-pulley	2N
MEL[c]	3	9	DC motor	tendon-sheath	N
Okada [1979]	3	11	DC motor	tendon-sheath	N
Stanford/JPL	3	9	DC motor	tendon-sheath	N+1
Toshiba[d]	4	16	DC motor	tendon-pulley/gear	N
Univ. of Bologna	3	11	DC motor	gear	N
Univ. of Kentucky	3	9	DC motor	tendon-pulley/gear	N
Utah/MIT	4	16	pneumatic	tendon-pulley	2N

---

[a] See Nakano et. al. [1984].
[b] See Jau [1992].
[c] See Maekawa et. al. [1992]
[d] See Hashimoto et. al. [1993].

Table 1.1: Classification of some prominent dextrous hands.

important reason for using such transmission systems is that they allow the actuators to be located remotely from the hand, thus reducing its size and mass. A short discussion of issues related to tendon-driven systems is presented in §1.4.

Table 1.1 classifies some prominent dextrous hands according to structure, actuator type and transmission system. The following few sections describe the features of several of the dextrous hands listed in Table 1.1.

1.1.1 The Utah/MIT Dextrous Hand

The Utah/MIT Dextrous Hand (Figure 1.2) represents a major effort in the study of machine-based dexterity (Jacobsen et al. [1984b]). Many papers have been published on the design of the various subsystems and control systems involved (see §1.2 for a review of previous UMDH research).

The UMDH consists of three 4-DOF fingers and an opposing 4-DOF thumb. Each finger has three parallel axis joints to provide curling motion and a proximal joint for

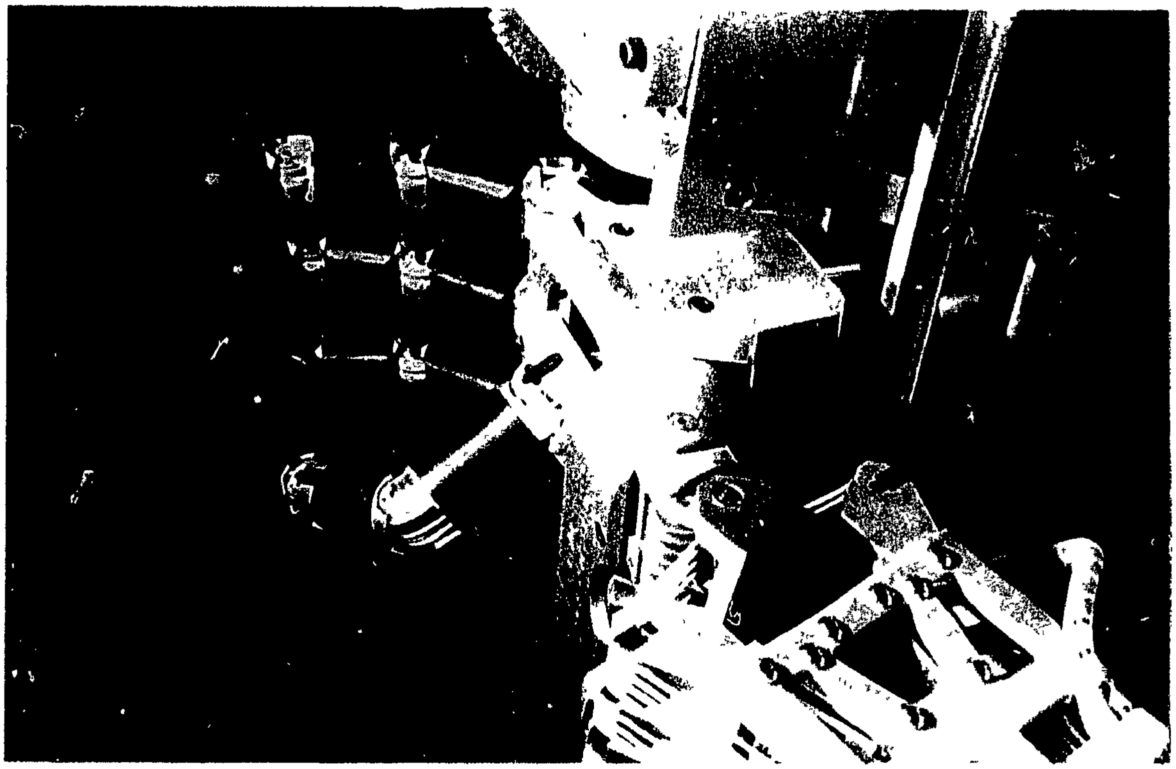

Figure 1.2: The Utah/MIT Dextrous Hand.

abduction/adduction motion. Each joint is controlled by two tendons and two linear, pneumatic actuators operating antagonistically, resulting in a dextrous hand system of high flexibility and complexity. The hand is remotely located from the actuator package by an ingenious pulley system called a "remotizer", which keeps the length of the tendons constant when the hand is moved about the workspace.

The first version of the hand featured two-stage, pressure-control, jet pipe valve actuators although these were changed to single-stage valves in the final version. Early tests of the performance of the hand revealed that the position bandwidth of the joints was as high as 8 Hz (Jacobsen et al. [1984c]).

1.1.2 The Stanford/JPL Hand

The Stanford/JPL Hand is an anthropomorphic end-effector intended for retrofit of existing manipulators (Salisbury and Craig [1982]). This hand consists of two 3-DOF fingers and a 3-DOF thumb for a total of 9-DOF. Each digit has two parallel axis joints and a third proximal joint to provide abduction/adduction motion. The actuation system is an $N+1$ type tendon-operated system where four tendons are used to control the three joints of each finger. In total, twelve Samarium-Cobalt DC torque motors with 28:1 gear reduction located on the forearm provide the actuation.

In Loucks et al. [1987], the modelling and control of the Stanford/JPL Hand is examined. In this paper, the researchers discuss model-based control for the hand. They also present mechanical hysteresis curves for the transmission system and propose a feedforward control system to reduce the effects of friction and hysteresis.

1.1.3 The Belgrade/USC Hand

The Belgrade/USC Hand (Venkataraman and Iberall [1990]) is an anthropomorphic end-effector with four fingers, one thumb, and four motors: one motor per finger pair and two for the thumb. Each finger including the thumb has three parallel axis joints without abduction/adduction capability. The fingers are designed with a self-adaptability feature that enables all the fingers to close until the pressure on all the finger pads is approximately equal, hence achieving local autonomy when grasping. Because the fingers and finger joints cannot operate independently, this hand is only able to perform simple grasping functions and therefore is not capable of fine manipulation tasks.

1.1.4 The Anthrobot-2 Dextrous Hand

The Anthrobot-2 Dextrous Hand (Ali et al. [1993]) is an anthropomorphic robotic hand constructed at NASA Goddard. This hand was specially designed for anatomical consistency with the human hand, including the shape of the palm, and the number, placement and motion of the fingers and thumb. Each finger, as well as the thumb, has four joints, although the distal joint of each robot finger is connected to the middle joint as in the human hand. Therefore, the Anthrobot-2 has a total of 16-DOF and hence has sixteen servomotors.

The fingers are tendon-driven, again simulating the structure of the human hand. Each servomotor has two tendons which control the flexion and extension of each joint. This configuration is the N-type, or one motor per joint.

1.1.5 The University of Bologna Robotic Hand

The University of Bologna has recently developed a tactile-sensor equipped dextrous hand for the study of dexterity in manipulation (Fantuzzi et al. [1992]). The version II prototype has two 4-DOF fingers and a 3-DOF thumb, for a total of 11-DOF. Each joint is remotely driven by a DC motor through 161:1 reduction gears, eliminating the need for tendons. Joint angles are measured using Hall-effect sensors.

One interesting feature of this hand is that each finger segment, as well as the palm, is instrumented with a modular, multicomponent force/torque sensor. These sensors provide information on the magnitude and location of acting wrenches during grasping and could possibly be used to detect slippage.

1.2 Previous Research Involving the Utah/MIT Dextrous Hand

In this section, a brief survey of research related to the Utah/MIT Hand is presented. As evidenced by the diversity of the research undertaken, it is clear that the hand has served its purpose as a general purpose research tool to investigate issues related to machine-based dexterity.

The first papers related to the UMDH covered design issues, in particular: motivation for the project, choice of anthropomorphic geometry, kinematic structure, and transmission and actuation system design (Jacobsen et al. [1984a], Jacobsen et al. [1984b], Jacobsen et al. [1984c], Jacobsen et al. [1986]). It is mentioned often in these

Figure 1.3: The Utah Dextrous Hand Master.

early papers that a viable, high-performance pneumatic actuator is extremely difficult to develop and critical to the project's success. In a more recent paper, Jacobsen et al. [1988] discuss the design of tactile sensing systems for dextrous manipulators such as the UMDH.

A series of publications (Siegel et al. [1985], Narasimhan and Siegel [1987], Narasimhan et al. [1988], Narasimhan [1988], Narasimhan et al. [1989]) describe the computational architecture of the real-time control system originally developed for use with the hand but also used to control the MIT Serial Link Direct Drive Arm, for example. The control system consists of a M68020 multiprocessor-based architecture with message-passing and shared memory capabilities. Narasimhan et al. [1986] describe the implementation of control methodologies on the UMDH computational architecture.

The UMDH has been featured in a variety of teleoperation efforts. For instance, Hong and Tan [1989] calibrated a VPL DataGlove for use with the UMDH. Pao and Speeter [1989] and Speeter [1992] discuss the transformation of human hand positions for robot hand control, using the UMDH as an illustrative example. In a more recent effort, Farry and Walker [1993] used myoelectric signals from the human hand to teleoperate the UMDH. Rohling and Hollerbach [1993] (see also Rohling et al. [1994]) recently developed an algorithm for teleoperating the UMDH in which human fingertip positions and orientations are mapped onto the UMDH, requiring a unique method for solving the inverse kinematics of the robot hand. In this work, the human fingertip positions are obtained from forward kinematics using the Utah Dextrous Hand Master (Figure 1.3) to measure joint angles. In a related work, Rohling and Hollerbach [1994] performed closed-loop calibration of the human index finger for improved teleoperation of robot hands.

The UMDH has also been an intrinsic part of many studies not specifically related to teleoperation. For instance, Speeter [1991] presents a method for dextrous manipulation of the UMDH using predefined sets of coordinated joint movements. Another study involving the UMDH was performed by Rockenbeck [1989] in which he performed static load estimation derived from tendon tensions and joint torques. Michelman and Allen [1993] studied compliant manipulation using the UMDH, addressing the problem of manipulating objects that are in contact with the environment. A software simulator which graphically portrays the grasps and tasks of the UMDH in operation is described in Perlin et al. [1989]. Bennett and Hollerbach [1990] performed closed-loop kinematic calibration of the UMDH. Allen et al. [1989] describe an integrated system for dextrous manipulation using the UMDH and a PUMA 560 manipulator facilitating the study of higher levels of control in a number of grasping and manipulation tasks. Allen and Roberts [1989] describe an effort at using the UMDH for haptic object recognition. Grupen [1991] discusses the problem of planning grasp strategies for multifingered robot hands and presents simulated grasping results using the UMDH hand geometry. Finally, an investigation of the tendon transmission system of the UMDH is given in Nahvi et al. [1994].

1.3 Dextrous Hand Actuation Systems

Dextrous hand systems employ a variety of actuator technologies (see Table 1.1). Each technology has its pros and cons in terms of power and torque capabilities, size, mass, cleanliness, and ease of operation. Therefore, the actuator type must be carefully chosen to match the performance criteria of the hand. To obtain human-like behavior, actuators must have extraordinary performance under active control, but also must be compliant when interacting with objects in the environment.

Electromagnetic motors are clean, compact and plentiful, although they tend to have a low torque/mass ratio (< 6 N·m/kg), thus requiring some sort of gear reduction in the power transmission system. Geared systems tend to have problems such as backlash and friction making stable, high performance control quite difficult (Townsend [1988]). Direct-drive motors have received considerable attention lately since they provide a means of actuating joints directly without intervening gears and have a higher torque/mass ratio (15 N·m/kg) than conventional DC motors. These motors are presently far too large for dextrous hands, although they have been used successfully on robot arms such as the MIT Serial Link Direct Drive Arm (An et al. [1988]).

Hydraulic actuators have large torque/mass and power/mass ratios compared to electromagnetic motors and therefore are often found in large robots and machinery. Problems associated with leakage, coupling, filtration and routing have traditionally kept hydraulic actuators from appearing in small applications such as dextrous hands. However, a force reflective hand master/slave recently developed by the Center for Engineering Design at the University of Utah (Jacobsen et al. [1989a]) has incorporated suspension-type, jet pipe valve hydraulic actuators.

Pneumatic actuators with sliding spool or suspension-type, jet pipe valves offer a clean and practical low-power alternative to hydraulics (Thayer [1984]). Pressure control is considerably superior to flow control in overcoming limitations of compressibility on bandwidth and stability, and hence the original pneumatic actuation system of the UMDII featured a two-stage, suspension-type, jet pipe valve which acted as a pressure control source. High performance, low-pressure systems such as this require tight tolerances to minimize leakage, and fast acting servovalves to reduce the effects of gas compressibility. However, the compressibility of the gas also has a beneficial effect in that it adds an intrinsic compliance to the system.

Recently a few dextrous hand systems employed SMA actuators. These actuators usually consist of coiled Nickel-Titanium (NiTi) fibers which contract when heated and return to their original shape when cooled. The heating mechanism is usually current, thus the contraction time for these fibers can be made very short. However, the expansion time for these fibers is significantly longer due to the length of time it takes to cool. Researchers have been attempting to improve the response time of NiTi fibers. For example, Hunter et. al. [1991] have improved the total contraction plus relaxation time of NiTi fibers by exposing them to massive electromagnetic fields. SMA actuators have a huge force per cross sectional area (> 200 MN/mm^2) and a large power/mass ratio (50 kW/kg). The lightweight and compact nature of these actuators makes them an interesting candidate for dextrous hands.

1.4 Tendon-Driven Systems

Due to severe constraints imposed on dextrous hands concerning size, strength and speed, actuators must often be relocated outside the hand. This raises the issue of how to transmit power from the actuators to the joints or links of the hand. Flexible tendons are a natural choice because of their low inertia, friction and backlash, as well for the reason this is what the human hand uses. Consequently, dextrous hands often incorporate a system of tendons and pulleys for power transmission, as opposed to geared or direct-drive systems.

Tendon-driven manipulators can be classified into three main categories based on the ratio of number of actuators employed to number of degrees-of-freedom (DOF). For an N-DOF manipulator, the three categories are N, $N+1$, and $2N$. Belt transmission systems are N-type since only one motor is required per joint. This type of transmission system is the most common of the three types due to its relatively low complexity. A drawback of this approach is that pretensioning is required to prevent slacking of the tendons during fast motions, resulting in undesirable friction and backlash. Transmission systems such as that employed on the UMDH require two actuators per joint and hence are called $2N$-type. In this configuration two tendons operate antagonistically to position each joint, thus requiring low co-contraction forces, although twice as many actuators are required. Evidently, each configuration has its own merits and weaknesses. In general, dexterity increases with the number of actuators used at the cost of added complexity. Jacobsen et al. [1989b] (see also Jacobsen et al. [1990]) provide an overview of tendon-driven systems and present efficient antagonistic control algorithms. Ko et al. [1990] describe a high stiffness and low slew drag antagonistic controller to be used in tendon-driven end-effectors.

Two types of methods exist to route the tendons from the actuators to the joints: pulleys and guide tubes (also known as tendon-sheaths or Bowden cables). Pulleys are attractive because they have lower friction than guide tubes, but require mounting surfaces and are less reliable. Guide tubes do not require any mounting surfaces, but introduce an unwanted source of friction and have slightly less flexible transmission pathways.

In Bejczy and Salisbury [1980], the basic mechanism and cable-drive system of a force-reflecting hand controller is described. In this paper, the authors stress the necessity of a low backlash, low friction, low inertia drive system to make the controller mechanism as transparent as possible to the user.

The low level control and tendon management scheme of the UMDH are discussed in Biggers et al. [1986]. In this paper, the authors state that future research involving the UMDH will include modelling of the actuation system and finger dynamics for use in model-based control.

Guo et al. [1992] present a new design for a 9-DOF dextrous robotic hand developed at the University of Kentucky using an N-type configuration; each joint uses a two-way tendon actuation system with only one motor.

Recently, researchers have studied the dynamics of tendons and the effects of friction in transmission systems. Johnstun and Smith [1992] modelled the dynamics of single tendons using transmission line models and concluded that pulley friction is primarily Coulombic. Kaneko et al. [1991] discuss force control for a tendon-sheath driving system typically used to actuate robotic finger joints. Kaneko et al. [1992] discuss the input-dependent stability of a robot finger joint using a tendon-sheath system and note that friction and compliance introduce a hysteresis nonlinearity between joint torque output and actuator displacement. In a paper discussing the efficiency of belt and cable drives, Townsend and Salisbury [1988] also note that friction must be minimized to reduce transmission losses and avoid stability problems.

Several research efforts have focused on the mechanical characteristics of different transmission systems. Townsend [1988] studied the effect of transmission design on force-controlled manipulator performance. In a later paper, Townsend and Salisbury [1989] introduce mechanical design strategies to improve performance, noting that much larger actuator torques are needed in a system with low mechanical bandwidth.

1.5 Model-Based Control

Model-based control is a control strategy whereby the dynamic response of a manipulator is predicted and accounted for. This method shows much promise in enabling better performance for robots. There are many texts discussing the application of model-based control, one of which is Craig [1989].

One example of model-based control for a dextrous hand can be found in Loucks et al. [1987], in which the authors formulate a dynamic model, including actuator dynamics, for the Stanford/JPL hand. In this paper the authors state that configuration-dependent inertia effects friction-based hysteresis can be minimized using model-based control,

A rigorous application of model-based control for a robot manipulator is found in An et al. [1988], in which the investigators use advanced techniques for identifying the kinematic and inertial parameters of the MIT Serial Link Direct Drive Arm in order to formulate an accurate dynamic model. Several model- and non-model-based control strategies are then compared with results showing that the best performance is obtained when using model-based control.

Actuator models play an integral role in model-based control since the generation of force or torque certainly has dynamics of its own. Furthermore, the sources of hysteresis may lie in the actuator as well as the transmission system, perhaps requiring a different method of compensation for each. This thesis develops a model of the actuation system of the UMDH, excluding the transmission system, as a step towards model-based control.

1.6 Actuator and Valve Modelling

Actuator modelling has received considerable attention in the past few decades. It has become clear that detailed knowledge of actuator properties is vital for improved performance in such advanced systems as robotic manipulators. Hence, a predictive dynamic model of an actuator is a very useful tool, whether to aid in the analysis and design of actuation systems, or for use in model-based control.

Although there are many textbooks covering the analysis of fluid flows, the following books are referred to frequently in the research literature because of their emphasis on the analysis of servosystems: Shapiro [1953], Blackburn et al. [1960], Burrows [1972] and Andersen [1976]. Terminology and specification standards for servovalves are presented in Thayer [1962], which are useful for interpreting manufacturing specifications and schematic diagrams. Funakubo [1991] contains a comprehensive survey of actuators for control as well as design fundamentals and applications.

Most of the early work focuses on the modelling of 4-way, spool valves using linear transfer functions. An analytical and experimental study was carried out by Shearer [1956] in which a linearized model for a pneumatic spool valve was derived for the midstroke position. Shearer [1957] performed an analog simulation comparing a linearized model and a nonlinear model incorporating Coulomb friction and concluded the main difference in frequency response was due to friction. Another linear analysis about the midstroke position was performed by Burrows and Webb [1967], this time using an on-off, flow control valve. Burrows [1969] expanded the work of Shearer to accommodate all ram positions but still used a transfer function approach. Botting et al. [1969] analyzed a 4-way, pneumatic spool valve using linear system theory and nonlinear digital simulation. As these investigators have noted, these linearized models are valid only for small fluctuations about a given operating point and therefore are only of limited use.

More recent studies involving 4-way, spool valves include the use of pressure feedback to improve control ('t Mannetje [1981]), experimental (Araki [1986]) and theoretical (Araki [1987]) frequency response determination, the use of the state-space approach to extend the linearized model over several operating points (Liu and Bobrow [1988]), and an application of adaptive control (Bobrow and Jabbari [1991]).

An excellent paper by Thayer [1984] provides a brief actuator technology comparison, and presents the relevant nonlinear equations for modelling an electropneumatic actuator in a concise format. The nonlinear dynamic model is then linearized about a mean operating point and the salient features are described. The paper also presents compensation techniques to improve performance.

Hydraulic actuators have also been analyzed using linear system theory. de Pennington et al. [1974] used linear transfer functions and curve-fitting to determine the optimum order linear model. Martin and Burrows [1976] compared the experimental and theoretical frequency response of a 2-stage, 4-way, hydraulic spool valve using models of varying complexity.

Recently, researchers have focused on developing comprehensive nonlinear models for the analysis of servosystems. For example, Bowns and Ballard [1972] performed a digital simulation of a pneumatic actuator using nonlinear equations to obtain the transient response. Shearer [1980] performed a digital simulation of a 4-way, hydraulic spool valve to show the effects of spool clearance, rounded corners and valve underlap. In a more recent paper, Handroos and Vilenius [1990] used low-order, nonlinear models to study single-stage, hydraulic pressure valves, in which the model parameters were identified with simple numerical methods using characteristic curves. In Wang and Singh [1986], the nature of the strong nonlinearities exhibited by pneumatic systems is examined. This work also includes an application of the method of harmonic balance and digital simulation to evaluate the frequency response of a pneumatic cylinder.

On-off, flow control valves have generated a lot of interest lately and have been shown to be very promising. Taft and Harned [1980] discuss the design of a low-power, 3-way, electropneumatic on-off valve. The speed and position control of a pulse-width-modulated, pneumatic on-off valve are covered in Noritsugu [1986] and Noritsugu [1987] respectively. Lai et al. [1990] also use pulse-width-modulation (PWM) control for an on-off, valve controller pneumatic actuator. In this paper, the authors state that PWM offers considerable advantages in the control of servos as it can reduce the effects of nonlinearities such as hysteresis and stiction. Kunt and Singh [1990] compare linear time-varying (LTV), linear time-invariant (LTI) and nonlinear models for an on-off, rotary control valve. In a later paper, Kunt and Singh [1992] used Floquet theory, based on an LTV model, to characterize the dynamic response of an pneumatic, on-off, spool valve.

Several studies which are of particular relevance to this thesis describe the modelling of jet pipe valve actuators. McLain et al. [1989] present a highly detailed model of a hydraulic actuator including the effects of friction, hysteresis, flow forces and piston damping. In this work, the authors use a hysteresis model based on a method described in Frame et al. [1982] (see also Talukdar and Bailey [1976]) which is capable of predicting minor loop trajectories based on the major loop and history of reversal points. A similar study was performed by Boulet et al. [1992], although with linear valve and fluid dynamics, and ARX identification. A Dahl friction model (Threlfall [1978]) is used, although all testing was performed with the piston locked at the mid-stroke position. Neither of these groups, however, include results on the effectiveness of the hysteresis model in predicting minor loops. An experimental and analytical investigation of the electropneumatic actuator studied in this thesis is presented in Henri and Hollerbach [1994].

For some background information on jet pipe elements, Aizerman [1968] contains some experimental and analytical studies, including the application of jet pipe elements for nonlinear transformations in pneumatic systems.

1.7 Statement of Work

This thesis presents the results of an analytical and experimental study of a suspension-type, jet pipe valve electropneumatic actuator designed for use in the Utah/MIT Dextrous Hand. This research represents the first step in an effort to characterize the dextrous hand system as a whole, and is intended to lay the foundation for the implementation of model-based control. Specific contributions include:

1. Development of a mathematical model of the actuator.
2. Identification of model parameters.
3. Detailed characterization of actuator components.
4. Verification of the model through simulation and experimentation.
5. Experimental results and simulation of force control using different control strategies.

6. Development of a linearized mathematical model which can be used to study stability and gain insight into how system parameters affect performance.

7. Comparison between the linearized and nonlinear models in closed-loop force control simulations.

2. Actuator Model

2.1 System Description

The electropneumatic actuator studied in this thesis was developed by Steve Jacobsen for use in the UMDH (Jacobsen et al. [1984a]) and consists of a single-stage, jet pipe valve attached to a glass cylinder housing a low-stiction graphite piston and steel rod (Figure 2.1). Current passing through the coil controls the position of the jet pipe which directs a high pressure air flow towards the orifices to each side of the piston. The pressure difference across the piston produces a force which is applied against a stopper on the end of the actuating rod. Since the piston can slide along the actuating rod, this actuator can only pull, not push. As part of the UMDH actuation system, two actuators operate antagonistically to servo each joint.

The actuation system of the UMDH features two different cylinder designs. The actuators controlling the two most distal joints for each finger use a single cylinder, as shown in Figure 2.1, whereas the actuators for the two most proximal joints incorporate a double-cylinder system. Table 2.1 lists the manufacturer's specifications for the single- and double-cylinder systems. The length, L, in Table 2.1 refers to the length indicated in Figure 2.1. The servovalve has a rated current of ± 0.4 A, a coil resistance of 9 Ω, and a rated no-load flow and maximum internal leakage of 0.000264 m^3/s and 0.000085 m^3/s respectively, at a supply (gauge) pressure of 689.5 kPa (100 psig).

Early versions of the UMDH featured a two-stage, pressure-controlling valve system consisting of a suspension-type jet pipe followed by a deflection jet pipe system positioned by antagonistic diaphragms (Figure 2.2), although commercial versions of the hand incorporate actuators using single-stage valves. The advantage of the suspension-type jet pipe valve design over conventional spool valves is that the moving mass is much less and hence faster servo rates are possible. Furthermore, the valve

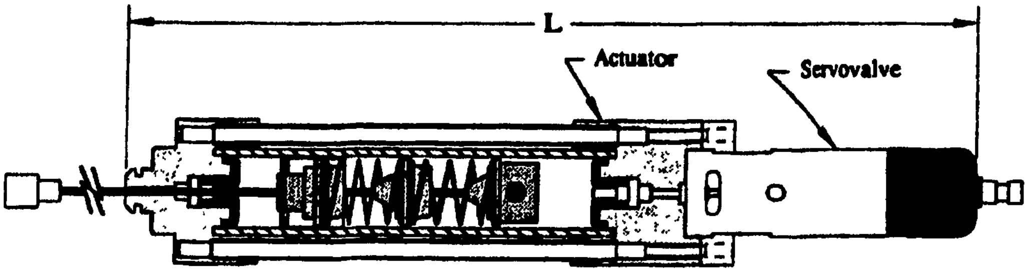

Figure 2.1: Electropneumatic actuator with single-stage jet pipe valve and single-cylinder assembly (Sarcos Research Corporation).

Cylinder Type	Bore Dia. (cm)	Stroke (cm)	Length, L (cm)	Max. Force (N)	Mass (g)
single	1.5875	5.08	18.77	111.25 @ 551.6 kPa[a]	131.5
double	1.5875	3.81	24.54	133.50 @ 551.6 kPa[a]	167.8

---

[a] supply pressure (gauge) (80 psig)

Table 2.1: Manufacturer's specifications for single- and double-cylinder pneumatic actuators.

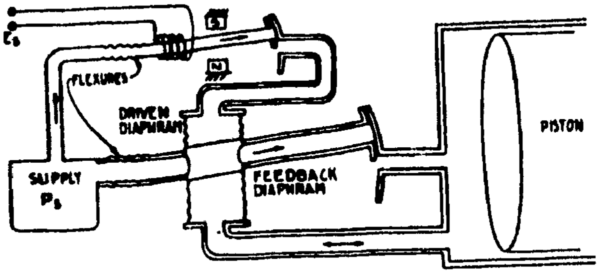

Figure 2.2: Early two-stage electropneumatic jet pipe valve designed for use in Utah/MIT Dextrous Hand (Jacobsen et al. [1986])

acts as a pressure source rather than a flow source, thereby avoiding oscillation problems caused by gas compressibility. Altogether, the valve and glass/graphite cylinder assembly results in a stable system with very low friction and mechanical impedance. A model for the two-stage valve is presented in Jacobsen et al. [1984a] along with experimental results and simulations. Their model represents the preliminary stage of the valve by two first-order lags: one for the response of the jet pipe to the input signal and the other for the charging of the primary diaphragm, whereas the model outlined here for the single-stage valve represents the jet pipe as a third-order system with a static nonlinearity. The rest of the model is essentially the same except for minor differences in the flow equations, orifice discharge coefficients and receiver plate offset.

Figures 2.3 and 2.4 show schematic diagrams of the servovalve and piston/cylinder assemblies for the single-stage, single-cylinder actuator. Figure 2.5 shows a block diagram of the actuator model.

The following sections examine each component of the actuator, outlining the relevant equations in the model.

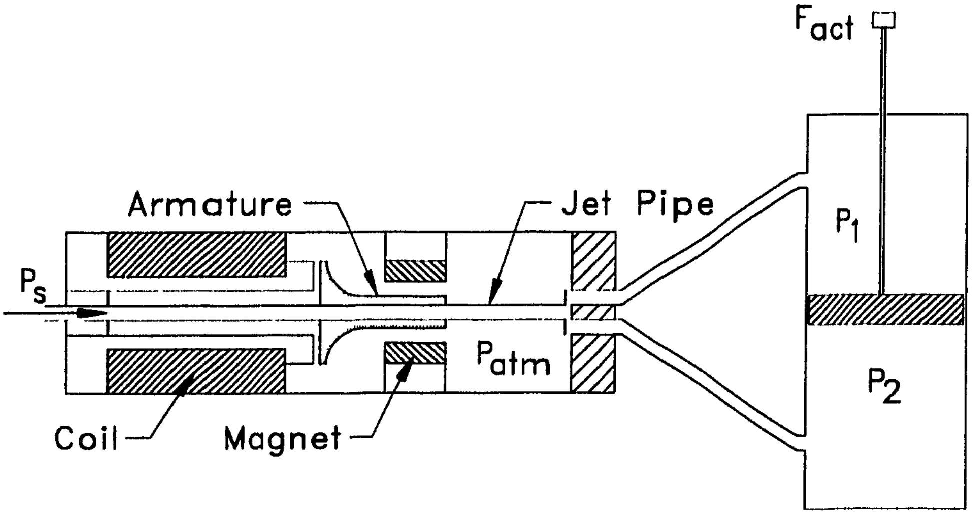

Figure 2.3: Schematic diagram of actuator with single-stage jet pipe valve.

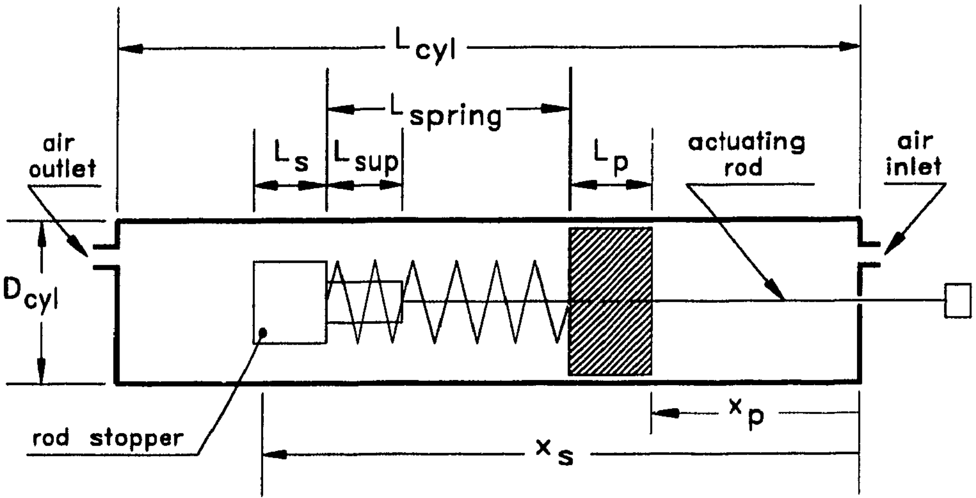

Figure 2.4: Schematic diagram of piston/cylinder assembly.

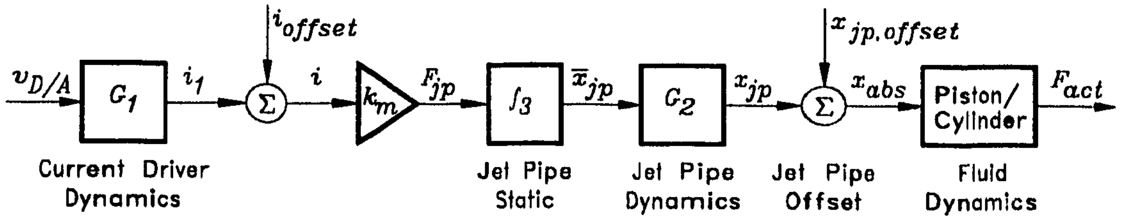

Figure 2.5: Block diagram of actuator model.

2.2 Current Driver

Current to the actuator is controlled via a voltage-to-current converter, or current driver, located on a joint controller card provided with the UMDH analog controller system. The current driver consists of an adjustable gain and offset with an RC low-pass filter. The command to the current driver is a voltage supplied by a D/A converter.

The inductance of the jet pipe coil has no effect on the current dynamics since it is cancelled out by the high gain of the amplifier in the closed-loop configuration. Therefore, as long as the system is driven under the saturation condition, the current driver acts as a first-order linear system.

The dynamics of the current driver are

$$G_1(s) = \frac{I_1(s)}{V_{D/A}(s)} = k_{cd}\left(\frac{\omega_{cd}}{s+\omega_{cd}}\right) \tag{2.1}$$

$$i_1 = i - i_{offset} \tag{2.2}$$

where i is the actuator current, i_{offset} is the adjustable offset, $v_{D/A}$ is the D/A converter voltage, k_{cd} is the adjustable current gain, and $\omega_{cd} = 1/RC$ is the corner frequency of the current driver first-order, low-pass filter.

The static input/output relation for the current driver is therefore

$$\bar{i} = k_{cd} v_{D/A} + i_{offset} \tag{2.3}$$

2.3 Jet Pipe

The jet pipe consists of a small diameter stainless-steel tube fixed at one end passing between a pair of permanent magnets. Current in the coil creates a magnetic field which magnetizes the jet pipe. The magnetized jet pipe interacts with the perpendicular flux lines of the permanent magnet such that the force on the pipe is proportional to current:

$$F_{jp} = k_m i \tag{2.4}$$

where F_{jp} is the effective force acting on the jet pipe tip, k_m is analogous to a "motor torque constant", and i is the actuator current. This force acts in a direction perpendicular to both the jet pipe axis and a line joining the permanent magnets.

Originally, it was thought to model the jet pipe as a second-order linear system in an attempt to capture the first bending mode. However, after experimentation it was found that this model did not accurately account for the observed nonlinear static behavior and the third-order roll-off in the frequency response. These results are presented in §3.2. A possible explanation is that the jet pipe is not fixed to the valve body in a cantilevered fashion, but rather is held in a sleeve containing some type of seal or o-ring with nonlinear characteristics. Although this explanation is speculative, that is, the exact physical reason for the additional first-order factor is unknown, the jet pipe is modelled as a third-order system with a static nonlinearity.

Based on frequency and step response tests, the dynamics of the jet pipe were found to be mostly independent of the static nonlinearity, indicating that the dynamics can be separated from the static characteristics. Furthermore, there was found to be a significant amount of hysteresis in the static position versus current relationship. Therefore, an attempt was made at modelling the jet pipe hysteresis using a model based on a method described by Frame et al. [1982]. The hysteresis model is described in §2.4, and some experimental results and simulations using the model are presented in §3.2.2.

The static nonlinearity relates jet pipe tip force to static tip position and is represented as

$$\bar{x}_{jp} = f_3(F_{jp}) \tag{2.5}$$

where $\bar{x}_{jp}$ is the static tip position for the given force on the jet pipe, and $f_3(F_{jp})$ is a function describing the static nonlinearity. In theory, the function $f_3(F_{jp})$ could be used to model the hysteresis effect, however experiments and simulations presented in §3.2.2 show that the model proposed by Frame does not adequately predict the minor loop trajectories. Therefore, the function $f_3(F_{jp})$ is taken to be the midpoint line of the experimentally obtained x_{jp} versus F_{jp} curve shown in Figure 3.5.

As previously stated, the dynamics of the jet pipe are third-order:

$$G_2(s) = \frac{X_{jp}(s)}{X_{jp}(s)} = \left(\frac{\omega_1}{s + \omega_1}\right)\left(\frac{\omega_2^2}{s^2 + 2\zeta_2\omega_2 s + \omega_2^2}\right) \tag{2.6}$$

where the terms ω_1 and ω_2 represent breakpoint frequencies to be experimentally determined from frequency response analysis. The term ζ_2 is the damping ratio for the second-order term, also to be experimentally determined.

To account for any misalignment between the jet pipe origin and the receiver plate center, the following offset is added:

$$x_{jp,abs} = x_{jp} + x_{jp,offset} \tag{2.7}$$

2.4 Hysteresis

As mentioned in the previous section, a significant amount of hysteresis exists in the jet pipe element (see §3.2.1). The source of this hysteresis lies in the force/current (i.e. magnetic flux) relationship of the coil as well as the mechanical position/force relationship of the jet pipe. This hysteresis has an adverse effect on actuator performance because the force output at a given current level varies depending on past inputs. Clearly, if the effects of hysteresis could be predicted, a suitable compensation

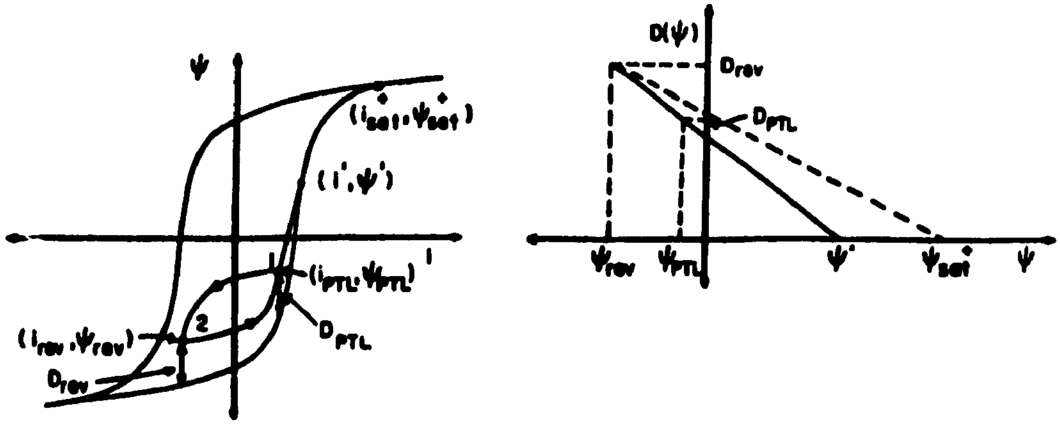

Figure 2.6: Hysteresis model proposed by Frame et al. [1982]. The subscripts "rev", "PTL" and "sat" refer to reversal, previous-to-last and saturation points.

could be performed to nullify these effects.

Two previous groups of investigators (McLain et al. [1989], Boulet et al. [1992]) which modelled hydraulic, suspension-type jet pipe valves similar to the pneumatic valve examined in this thesis included a model to account for the effects of hysteresis. This model is based on a method described in Frame et. al. [1982], which in turn is based on a method described in Talukdar and Bailey [1976]. This method attempts to predict minor loop trajectories based on the major loop and previous reversal points. The thrust of this method is that the distance between an increasing minor loop trajectory and the bottom (i.e. increasing) half of the major loop should decrease linearly with the ordinate (Figure 2.6). Likewise, the distance between a decreasing minor loop trajectory and the top (i.e. decreasing) half of the major loop should also decrease linearly with the ordinate.

2.5 Orifice Areas

The orifice areas through which fluid flows in or out of a control port are calculated from the geometrical overlap of the jet pipe and control ports. The small clearance between the jet pipe tip and the receiver plate does not appear explicitly in the model,

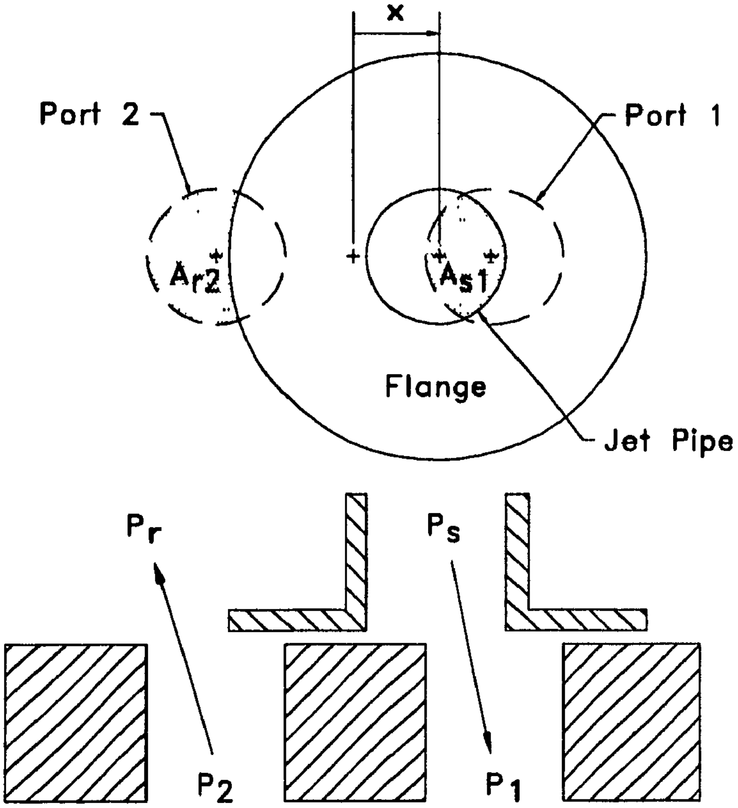

Figure 2.7: Orifice areas.

but rather is lumped into the discharge coefficient.

The control ports of the receiver plate are of the same diameter as the jet pipe exit area and are spaced one diameter apart. The jet pipe tip has a flange which serves to cover the opposite control port when the pipe is directed away from center. The diameter of the flange is three times the diameter of the jet pipe exit area, which just covers the control ports when the pipe it centered. A diagram of the orifice areas and their naming convention is shown in Figure 2.7. Port 1 is connected to the charging side of the piston and port 2 is connected to the venting side of the piston. P_s and P_r indicate the supply and return pressures respectively. Note that in this configuration, the return area for port 1, A_{r1}, and the supply area for port 2, A_{s2} are both covered by the jet pipe tip flange and hence are zero.

The orifice area equations are shown below. These in turn use some additional equations and parameters for ease of writing. Note that x refers to the position of the jet pipe tip relative to the receiver plate center, and A_{jp}, D and R refer to the jet pipe exit area, diameter and radius respectively.

Orifice supply area 1, A_{s1}:

$$A_{s1} = \begin{cases} 0 & \text{for } x \leq 0 \\ 2f_a(\left|\frac{D-x}{2}\right|, R) & \text{for } 0 \leq x \leq 2D \\ 0 & \text{for } 2D \leq x \end{cases} \tag{2.8}$$

Orifice return area 1, A_{r1}:

$$A_{r1} = \begin{cases} A_{jp} & \text{for } x \leq -D \\ f_{r1}(x - D) & \text{for } -D \leq x \leq 0 \\ 0 & \text{for } 0 \leq x \leq 2D \\ f_{r2}(x - D) & \text{for } 2D \leq x \leq 3D \\ A_{jp} & \text{for } 3D \leq x \end{cases} \tag{2.9}$$

Orifice supply area 2, A_{s2}:

$$A_{s2} = \begin{cases} 0 & \text{for } x \leq -2D \\ 2f_a(\left|\frac{D-x}{2}\right|, R) & \text{for } -2D \leq x \leq 0 \\ 0 & \text{for } 2D \geq x \end{cases} \tag{2.10}$$

Orifice return area 2, A_{r2}:

$$A_{r2} = \begin{cases} A_{jp} & \text{for } x \leq -3D \\ f_{r1}(x + D) & \text{for } -3D \leq x \leq -2D \\ 0 & \text{for } -2D \leq x \leq 0 \\ f_{r2}(x + D) & \text{for } 0 \leq x \leq D \\ A_{jp} & \text{for } D \leq x \end{cases} \tag{2.11}$$

Additional equations for orifice areas:

$$
\begin{aligned}
f_a(a,r) &= r^2\cos^{-1}\left(\frac{a}{r}\right) - a\sqrt{r^2-a^2} && (2.12)\\
f_b(b,r) &= r^2\sin^{-1}\left(\frac{b}{r}\right) - b\sqrt{r^2-b^2} && (2.13)\\
f_{r1}(c) &= \begin{cases} A_{jp} - f_b(d,R) - f_b(d,3R) & \text{for } u \geq 0 \\ f_b(d,R) - f_b(d,3R) & \text{for } u < 0 \end{cases} && (2.14)\\
f_{r2}(c) &= \begin{cases} f_b(d,R) - f_b(d,3R) & \text{for } u \geq 0 \\ A_{jp} - f_b(d,R) - f_b(d,3R) & \text{for } u < 0 \end{cases} && (2.15)
\end{aligned}
$$

where

$$
\begin{aligned}
u &= \frac{D^2}{c} - \frac{c}{2} && (2.16)\\
d &= \sqrt{R^2-u^2} && (2.17)
\end{aligned}
$$

2.6 Flow Equations

Assuming the flow processes are adiabatic, the mass flow rates through the orifices are governed by the following set of equations (Andersen [1976], Blackburn et. al. [1960], Thayer [1984]):

$$
\begin{aligned}
\dot{m} &= \begin{cases} C_dA\left(\frac{P_u}{\sqrt{T_u}}\right)C_1 & \text{for } \left(\frac{P_d}{P_u}\right) \leq r_c \text{ (choked)} \\ C_dA\left(\frac{P_u}{\sqrt{T_u}}\right)C_2f_2 & \text{for } \left(\frac{P_d}{P_u}\right) > r_c \text{ (non-choked)} \end{cases} && (2.18)\\
r_c &= \left(\frac{P_d}{P_u}\right)_{cr} = \left(\frac{2}{\gamma+1}\right)^{\frac{\gamma}{\gamma-1}} && (2.19)\\
C_1 &= \sqrt{\frac{\gamma}{R}\left(\frac{2}{\gamma+1}\right)^{\frac{\gamma+1}{\gamma-1}}} && (2.20)\\
C_2 &= \sqrt{\frac{\gamma}{R}\left(\frac{2}{\gamma-1}\right)} && (2.21)
\end{aligned}
$$

$$f_2 = \sqrt{\left(\frac{P_d}{P_u}\right)^{\frac{2}{\gamma}} - \left(\frac{P_d}{P_u}\right)^{\frac{\gamma+1}{\gamma}}} \tag{2.22}$$

where P_u and P_d are the upstream and downstream pressures, T_u is the upstream temperature, γ is the isentropic exponent for air (= 1.4), R is the gas constant for air (= 287 j/kg·K), $(P_d/P_u)_{cr}$ is the critical pressure ratio for air at which the flow changes from subsonic to sonic (= 0.528), A is the orifice area, and C_d is the orifice discharge coefficient.

The actuator is designed to be slightly "leaky" allowing a small flow between the chambers past the position. This leakage area is ring shaped and is long relative to its opening width indicating that the discharge coefficient should be a function of pressure ratio (Andersen [1976]), instead of a constant as is the case with the other orifices. Therefore, the discharge coefficient for the leakage past the piston area, A_{lpp}, is

$$C_{d,lpp} = C_{dm}\left(\frac{P_d}{P_u}\right) + C_{db} \tag{2.23}$$

where C_{dm} and C_{db} are constants.

The net mass flow rates for chambers 1 and 2 are

$$\dot{m}_1 = \dot{m}_{s1} - \dot{m}_{r1} - \dot{m}_{lpp} \tag{2.24}$$

$$\dot{m}_2 = \dot{m}_{s2} - \dot{m}_{r2} + \dot{m}_{lpp} \tag{2.25}$$

where the orifice area for $\dot{m}_{s1}$ is A_{s1}, for $\dot{m}_{r1}$ is A_{r1}, and the positive sense for $\dot{m}_{lpp}$ is from chamber 1 to chamber 2.

The net volumetric flow rate is simply the mass flow rate divided by the density. For chamber i, $i = 1, 2$, this becomes

$$Q_i = \frac{\dot{m}_i}{\rho_i} \tag{2.26}$$

where the density ρ_i is obtained from the ideal gas law:

$$\rho_i = \frac{P_i}{RT_i} \tag{2.27}$$

The adiabatic relation for temperature in chamber 1 is

$$T_1 = T_s\left(\frac{P_1}{P_s}\right)^{\frac{\gamma-1}{\gamma}} \tag{2.28}$$

where P_s and T_s are the supply pressure and temperature respectively.

However, because of the moderate pressures and temperatures involved, the model is simplified by assuming that temperatures do not vary appreciably from their nominal values and therefore are assumed to be constant. This assumption has been used previously by several investigators (Burrows and Webb [1967], Jacobsen et al. [1984a], Kunt and Singh [1990], Lai et al. [1990]). In fact, a study by Kawakami et al. [1988] revealed little difference in response of a pneumatic cylinder model whether the pneumatic processes are assumed isothermal or adiabatic. Nonetheless, the isentropic flow equations are presented here for completeness. In reality, the flow processes lie somewhere between isothermal and isentropic, although in a fast-acting system such as this, heat transfer is likely to be relatively small.

The rate of change of pressure in each chamber is given by

$$\dot{P}_i = \frac{\gamma P_i}{V_i}\left(Q_i - \dot{V}_i\right) \tag{2.29}$$

where V_i is the volume of chamber i, and $\dot{V}_i$ is the rate of change of volume of the chamber. Note that this equation is obtained from the first derivative of the ideal gas law assuming an adiabatic process.

Neglecting the small volumes of the rod stopper and support (see Figure 2.4), the chamber volumes, V_1 and V_2, are given by

$$\begin{aligned} V_1 &= A_p x_p \qquad (2.30) \\ V_2 &= A_p(L_{cyl} - x_p - L_p) \qquad (2.31) \end{aligned}$$

where A_p is the piston area, x_p is the piston position, L_p is the piston length, and L_{cyl} is the cylinder length.

The supply pressure, P_s, is assumed to be constant and acts at the outlet of the jet pipe tip. Furthermore, the fluid lines after this point are all short and inflexible, and hence line resistance, capacitance and inertance are all assumed negligible.

2.7 Piston Dynamics

The piston inside the cylinder is spring loaded and slides along the actuator rod between the rod stopper and the end of the cylinder. This arrangement maintains residual tension in the tendons when the system is unpressurized, preventing tendon misalignment. When the pressure difference across the piston is sufficiently high, the spring becomes fully compressed and the piston contacts the rod stopper. The spring has a low spring constant and hence the piston contacts the rod stopper for all but extremely low actuator forces. Therefore, the piston is assumed to be stuck to the rod stopper (see Figure 2.4). That is, the piston and stopper positions differ by the sum of the piston, stopper and support lengths:

$$x_p = x_s - (L_p + L_s + L_{sup}) \qquad (2.32)$$

where L_p, L_s and L_{sup} are the piston, stopper and support lengths respectively.

Lumping the mass of the stopper and piston together, and assuming viscous damping yields

$$m_p \ddot{x}_p + b_p \dot{x}_p + F_{act} = F_p - F_f \qquad (2.33)$$

where the subscript p refers to the piston, F_p is the force on the piston due to the pressure differential, and F_f is the dry friction force:

$$
\begin{aligned}
F_p &= A_p(P_1 - P_2) && (2.34)\\
F_f &= \begin{cases} F_c \mathrm{sgn}(\dot{x}_p) & \text{for } \dot{x}_p \neq 0 \\ F_p & \text{for } \dot{x}_p = 0, F_p < F_s \\ F_s \mathrm{sgn}(F_p) & \text{for } \dot{x}_p = 0, F_p \geq F_s \end{cases} && (2.35)
\end{aligned}
$$

where F_c and F_s are constants equal to the Coulomb friction force and stiction force respectively.

Friction between the graphite piston and glass cylinder is known to be small (Jacobsen et al. [1986]) and is further reduced by the lubricating effect of the air flow past the piston. Friction between the rod and cylinder seal is assumed insignificant as well, meaning that stiction and kinetic friction are neglected entirely. Furthermore, the dynamics of the load are expected to dominate those of the lightweight, low-friction, graphite piston which means that for all practical purposes the piston dynamics can be neglected. Therefore, the actuator force is

$$F_{act} = A_p(P_1 - P_2) \qquad (2.36)$$

with the minimum actuator force equal to the residual spring force when the piston contacts the top end of the cylinder. Referring to Figure 2.4, the spring force with $x_p = 0$ is

$$
\begin{aligned}
F_{spring} &= k_{spring}(L_{spring,0} - L_{spring}) && (2.37)\\
L_{spring} &= x_s - L_s - L_p && (2.38)
\end{aligned}
$$

where $L_{spring,0}$ is the unloaded length of the spring.

3. System Identification

3.1 Current Driver

3.1.1 Static Characteristics

Identification of the current driver characteristics was separated into static and dynamic parts. The static gain and offset are adjustable via potentiometers located on the joint controller cards in the UMDH analog controller system. These parameters were determined by measuring the voltage drop across a precision resistor placed in series with the actuator (Figure 3.1). Referring to (2.3), the static current supplied by the current driver, $\bar{i}$, was easily calculated for each voltage command from the D/A using

$$\bar{i} = \frac{v_{test}}{R_{test}} \tag{3.1}$$

where v_{test} is the measured voltage drop across the precision resistor, and R_{test} is the resistor's known resistance. A straight line was then fit to the data to obtain the gain and offset. As mentioned previously, these parameters are variable and hence this procedure was repeated whenever the gain and offset were adjusted.

3.1.2 Dynamic Characteristics

The dynamics of the current driver were determined using a swept sine frequency response test (Figure 3.2) with D/A voltage as the input and current (measured indirectly as above) as the output. An HP 35665A dynamic signal analyzer was used to automate the procedure. As expected, the response was first order low-pass, with a corner frequency of 1122 Hz. This compares with the theoretical value of 1592 Hz resulting from a 10 KΩ resistor and a 0.01 μF capacitor. The capacitor and resistor values have fairly large uncertainties so this discrepancy is not unreasonable.

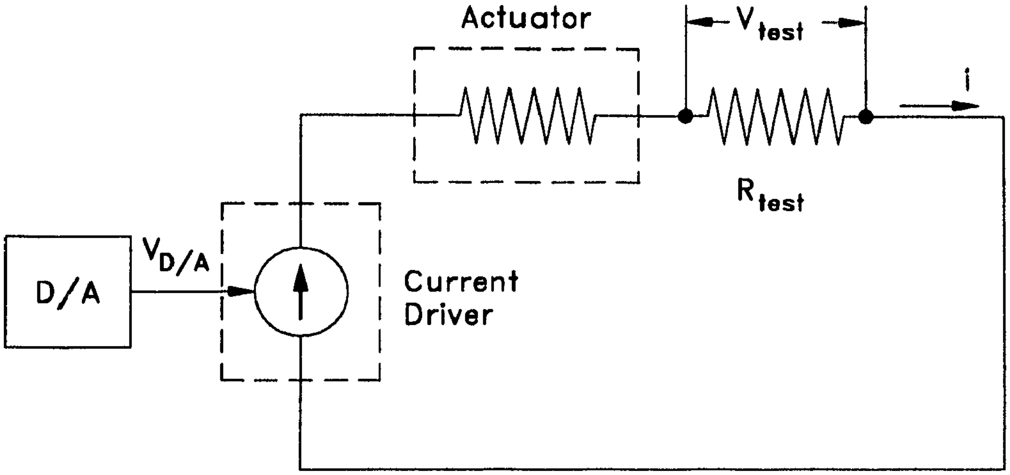

Figure 3.1: Method for measuring current to determine driver gain and offset.

Referring to (2.1), the parameter ω_{cd} is therefore 7050 rad/s.

Note that the actuator is in the loop (Figure 3.1) during the current driver tests. The inductance effect of the actuator coil on the current dynamics is cancelled out by the high gain of the current driver amplifier and hence the dynamics of the current driver are a result of the first-order, low-pass filter alone.

3.2 Jet Pipe

3.2.1 Static Characteristics

To measure the position of the jet pipe, a miniature HP HEMT-6000 light emitting diode (LED) was attached to the tip of the jet pipe and its position was sensed by a SiTek J1L photosensitive detector (PSD). The apparatus was calibrated by deflecting the jet pipe tip with a probe attached to a micrometer plunger and recording the corresponding output of the PSD. A photograph of the experimental setup appears in Figure 3.3.

By slowly ramping the current up and down until the position saturated, the characteristic major hysteresis loop was obtained (Figure 3.4).

To determine the source of the hysteresis, mechanical testing was performed on

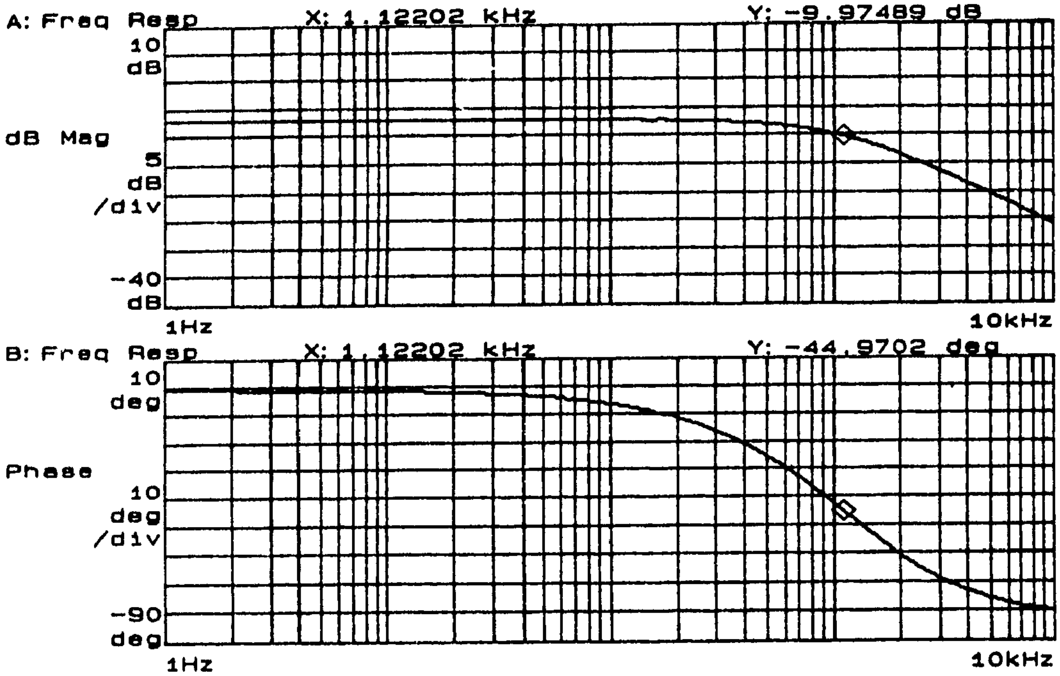

Figure 3.2: Current driver frequency response: $I(j\omega)/V_{D/A}(j\omega)$

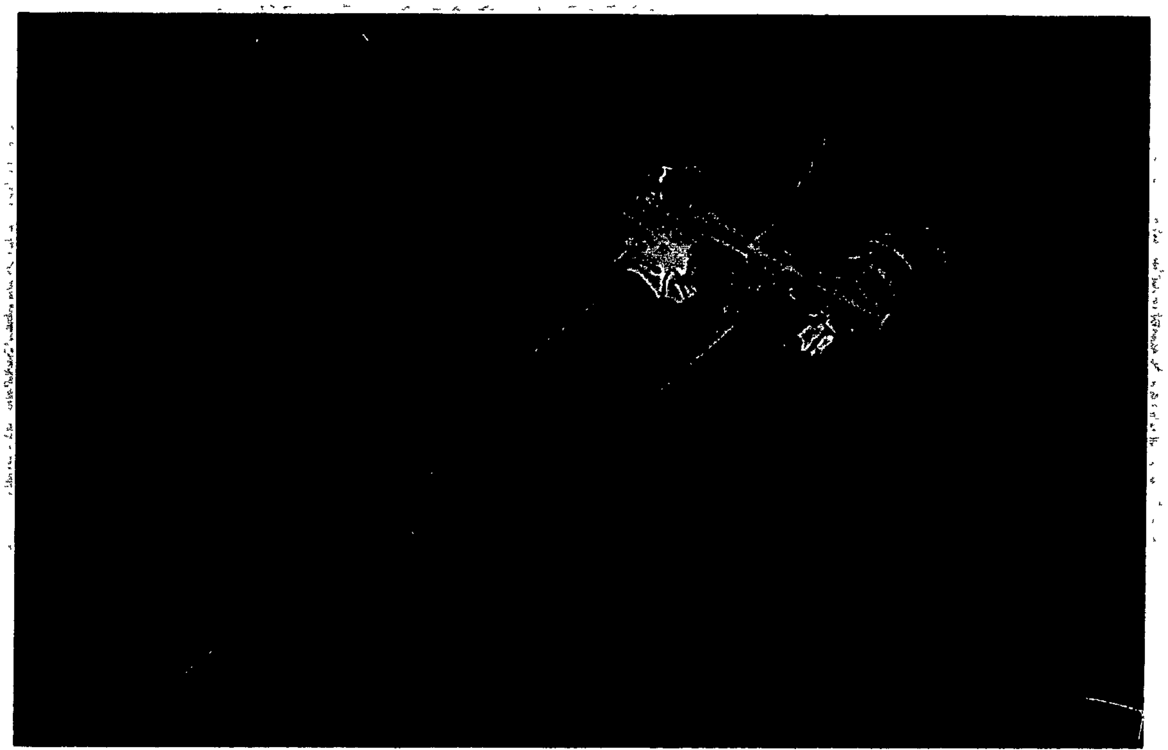

Figure 3.3: Photograph of apparatus used to measure jet pipe position.

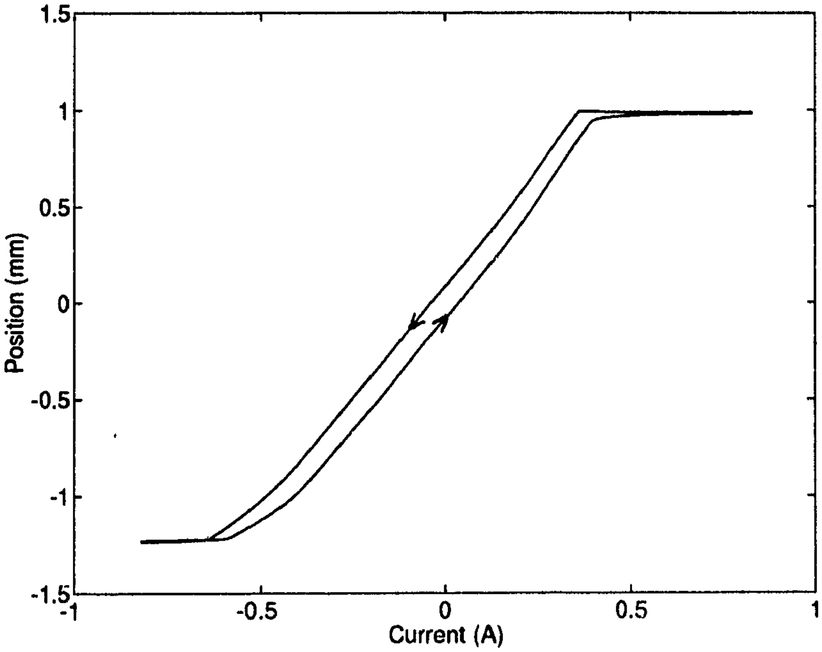

Figure 3.4: Jet pipe position vs. current.

the jet pipe by applying forces directly on the jet pipe tip via hanging masses. Due to limitations in the experimental apparatus, it was possible to deflect the jet pipe downwards only. From the position/current curve (Figure 3.4) and the left half of the position/force curve (Figure 3.5) it was possible to derive the bottom half of the force/current curve (Figure 3.6). The force/current curve was reasonably assumed to be symmetric for positive force and current, permitting the derivation of the right half of the position/force curve. Since the effects of hysteresis are not directly accounted for in the system model, the nonlinear function $f_3(F_{jp})$ in (2.5) is simply the midpoint line of the position/force curve.

Notice that the force/current curve (Figure 3.6) shows only a slight amount of hysteresis and is remarkably linear within the actuator's rated current limits of ± 0.4 A. The best fit for this operating range gives a motor torque constant, k_m, equal to 1.946 N/A, with a standard deviation of 0.007 N, and is indicated by the dashed line. It is surprising that the force/current (i.e. magnetic flux) relationship of the coil is not

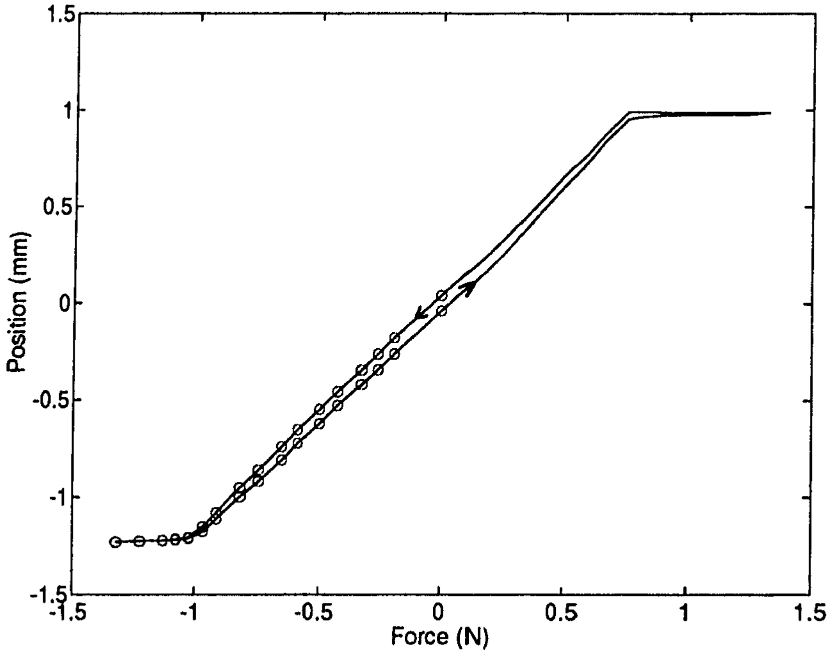

Figure 3.5: Jet pipe position vs. tip force.

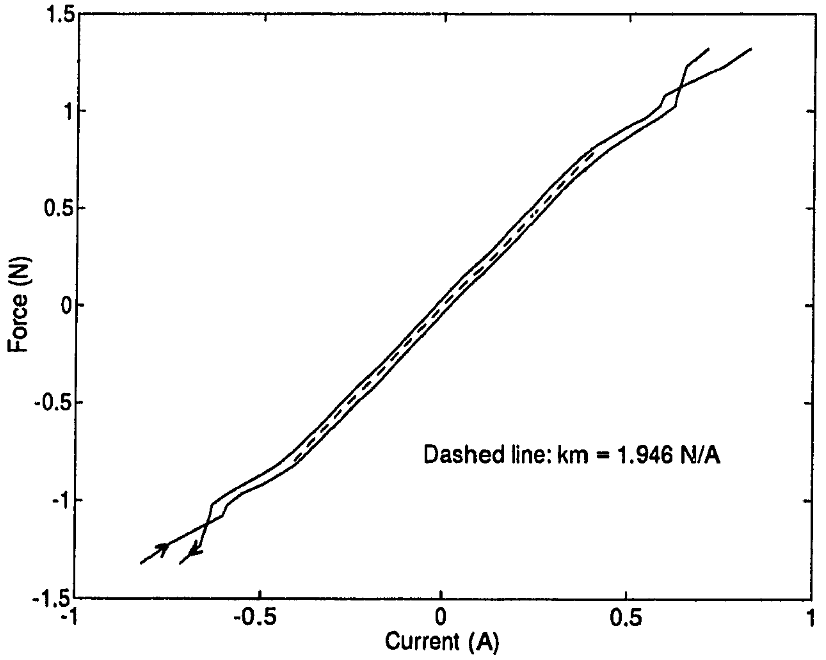

Figure 3.6: Jet pipe tip force vs. current.

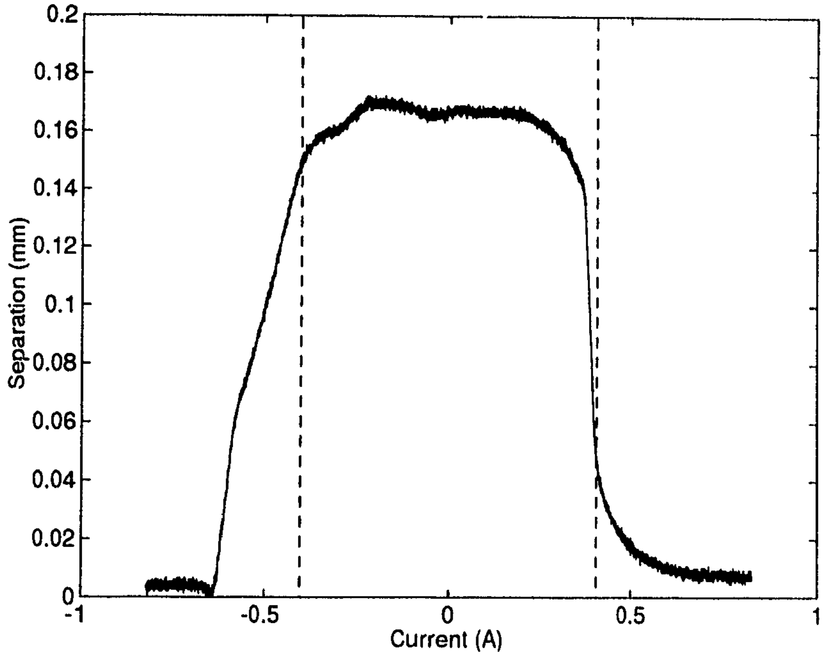

Figure 3.7: Separation between major loop halves for jet pipe position vs. current.

the sole source of hysteresis — Figure 3.5 clearly shows that there exists a significant amount of hysteresis in the position/force relationship as well. It is for this reason that a seal or o-ring around the jet pipe was hypothesized, having nonlinear stiffness and hysteretic characteristics.

The separation between the halves of the jet pipe position/current major hysteresis loop is almost constant in the operating range (Figure 3.7) at ≈ 0.16 mm. Therefore, comparing the distance between the midpoint line and the major loop, 0.08 mm, to the jet pipe operating range, 1 mm, gives a hysteresis of approximately 8 %.

3.2.2 Hysteresis — Minor Loop Trajectories

Several tests were performed on the jet pipe to verify the effectiveness of the hysteresis model shown in §2.4 at predicting the trajectories of minor loops. Figure 3.8a shows an experimentally obtained minor loop trajectory along with the trajectory predicted by the model. Using the terminology employed by Frame, the previous-to-

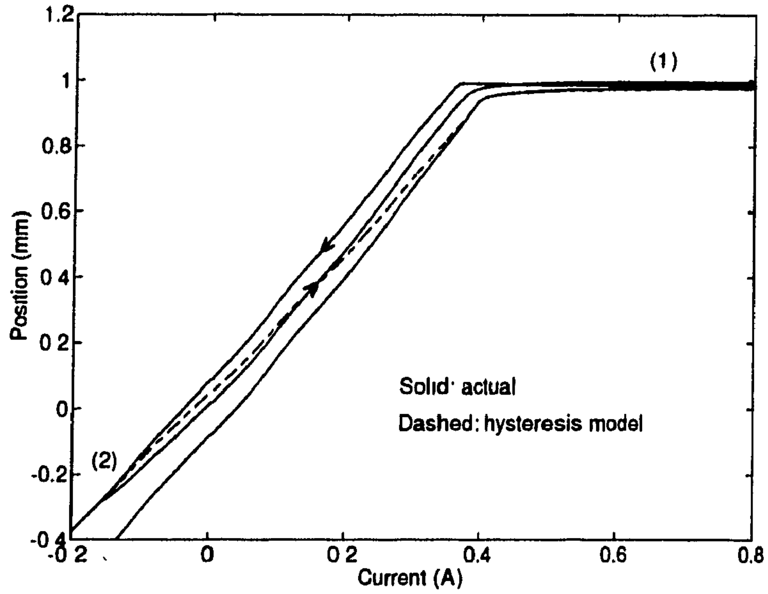

(a) Jet pipe minor loop trajectory #1

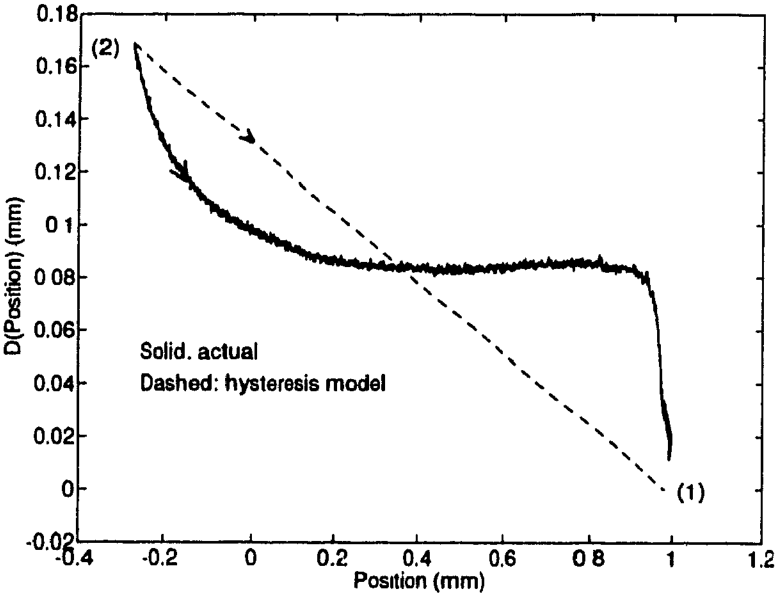

(b) Hysteresis model error for trajectory #1

Figure 3.8: Jet pipe hysteresis trajectory and model error #1.

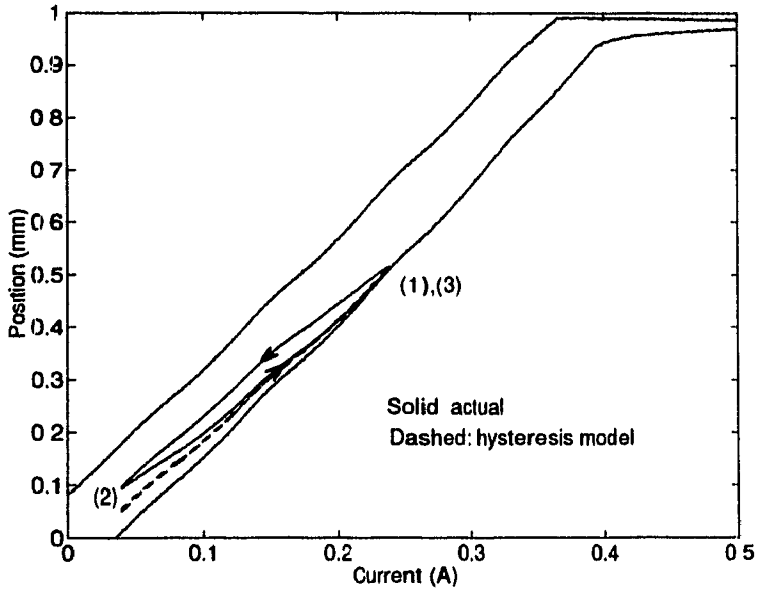

(a) Jet pipe minor loop trajectory #2

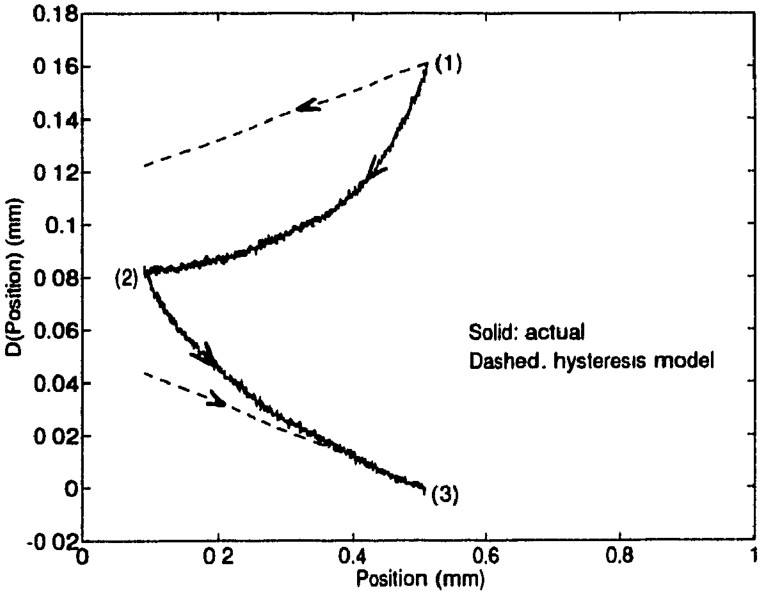

(b) Hysteresis model error for trajectory #2

Figure 3.9: Jet pipe hysteresis trajectory and model error #2.

last reversal point is indicated as **(1)** and the last reversal point is indicated as (2). The results show a significant error between the actual and predicted trajectories. Figure 3.8b clearly shows that the actual distance between the minor and major loops, denoted as D(Position), is very nonlinear. Figure 3.9 shows the same for a different minor loop trajectory. In fact, for repeated reversals, the hysteresis model was found to predict the minor loop trajectories with an accuracy no better than the midpoint line of the major loop. For this reason the nonlinear function $f_3(F_{jp})$ in (2.5) relating the static jet pipe position to force on the jet pipe tip was chosen to be the midpoint line of the position/force curve.

3.2.3 Dynamic Characteristics

A swept sine frequency response test was performed to identify the parameters of the third-order jet pipe model presented in §2.3. The results show that a third-order model fits the data well for frequencies below $\approx$ 700 Hz. The strange behavior of the system above 700 Hz can likely be attributed to saturation of the current amplifier due to the inductive nature of the coil. Figure 3.10 shows the experimental data and the third-order theoretical model. Referring to (2.6), the identified parameters are: $\omega_1 = 973.9$ rad/s (155.0 Hz), $\omega_2 = 1856.7$ rad/s (295.5 Hz), and $\zeta_2 = 0.019$.

A step response test confirmed the correctness of the model parameters. Figure 3.11 shows a sample step response along with the model response. The jet pipe is highly underdamped with a rise time of 0.002 s and a 5 % settling time of 0.07 s.

3.3 Actuator Response

The experimental apparatus used to obtain the actuator force/current characteristics consisted of a compact Entran ELF-TC500-100 force sensor which was rigidly fixed to a plate attached to UMDII actuator package (Figure 3.12). The simplicity of this setup enabled the use of the air supply, current driver and tendon connectors which are used during normal operation of the hand, and allowed different actuators

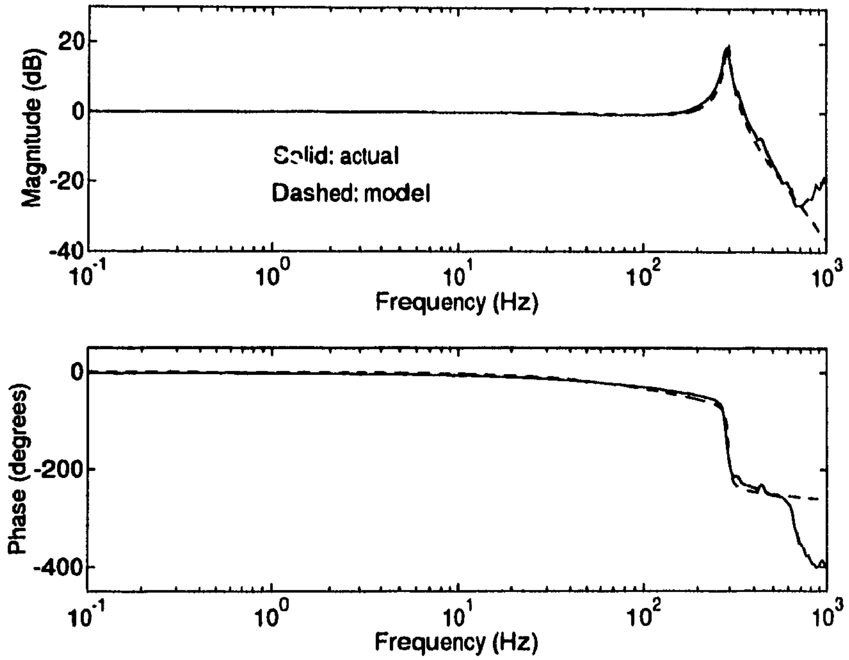

Figure 3.10: Jet pipe frequency response: $X_{jp}(j\omega)/X_{jp}(j\omega)$

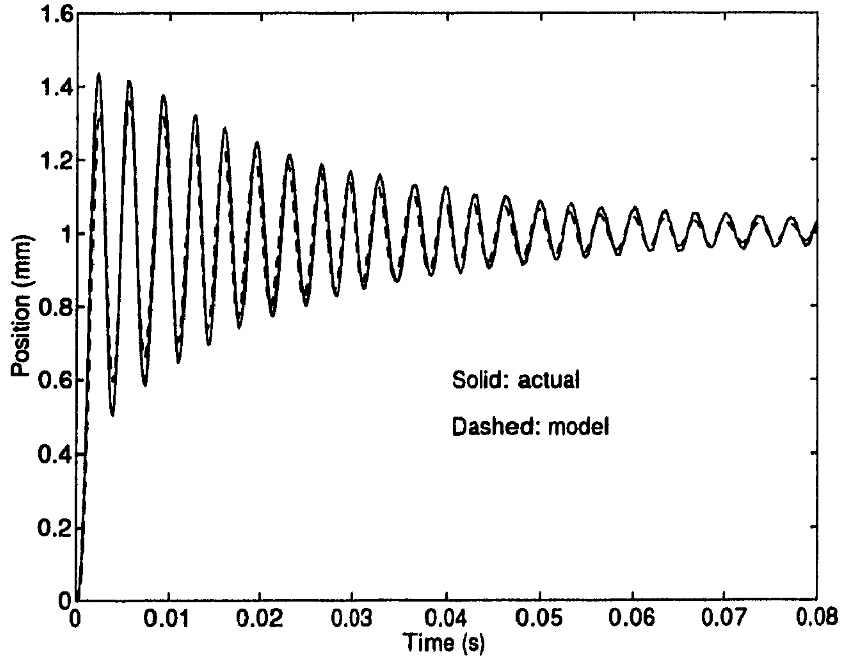

Figure 3.11: Jet pipe step response.

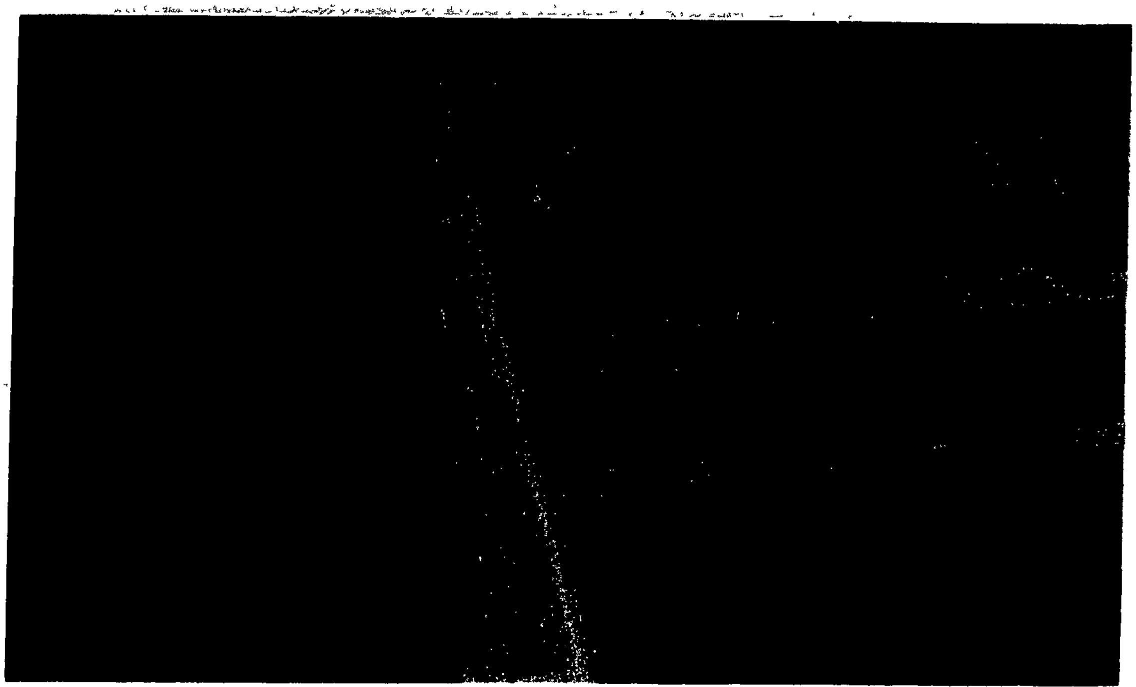

Figure 3.12: Photograph of apparatus used to measure actuator force.

to be tested without removal from the actuator package. Adjustable spacers between the force sensor and mounting plate permitted different rod stopper positions to easily be tested. An Entran PS-30A power supply/amplifier was used to power the sensor and amplify the signal.

3.3.1 Static Characteristics

Figure 3.13 shows the actuator major hysteresis loop which was obtained by slowly ramping the current up and down to the force saturation points. The procedure was automated by using the Condor real-time control system (Narasimhan and Siegel [1987]) driving Data Translation 12-bit D/A and 16-bit A/D boards. This test was repeated for several different rod stopper positions and confirmed that the static actuator force does not depend on the relative volume of the cylinder chambers. The model data uses the jet pipe position/current major hysteresis loop data shown in

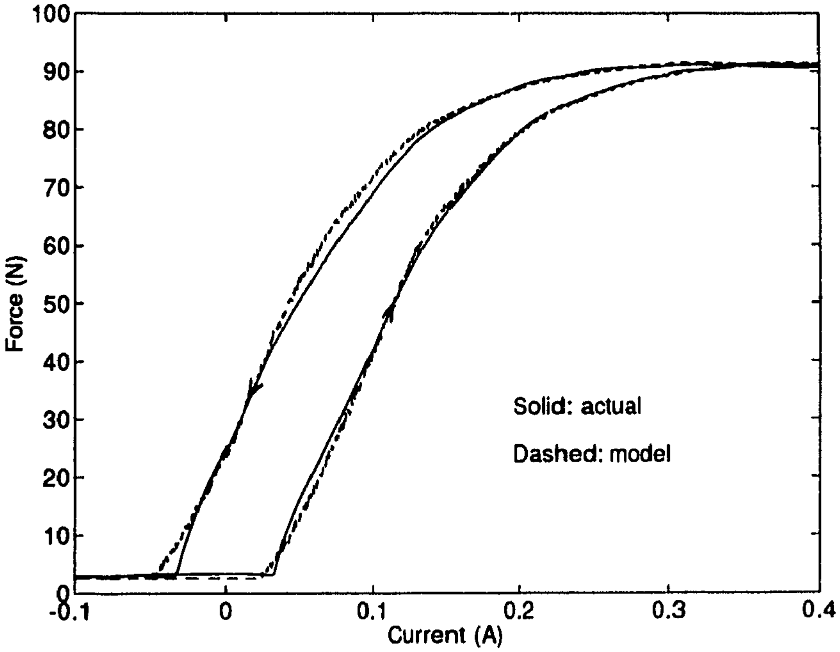

Figure 3.13: Actuator force vs. current.

Figure 3.4, and is indicated by a dashed line. Using the actuator force/current data and the jet pipe position/current data, the actuator force/jet pipe position curve was derived (Figure 3.14). The increasing and decreasing portions of the major hysteresis loops both yielded the same force/jet pipe position curves, as should be the case.

The non-zero minimum actuator force is due to the spring inside the cylinder (see Figure 2.4), which is designed to maintain a residual force in the tendons in order to prevent tendon misalignment when the system is unpressurized. The spring rate, k_{spring}, was determined by varying the spring length and recording the change in actuator force, with the air supply turned off. This value was calculated to be 88.14 N/m.

The only other model parameters which needed to be identified were the orifice discharge coefficients and the receiver plate offset. These parameters were identified by minimizing the sum of the squared errors between the experimental and theoretical actuator force/current major hysteresis loops. The model used the experimental jet

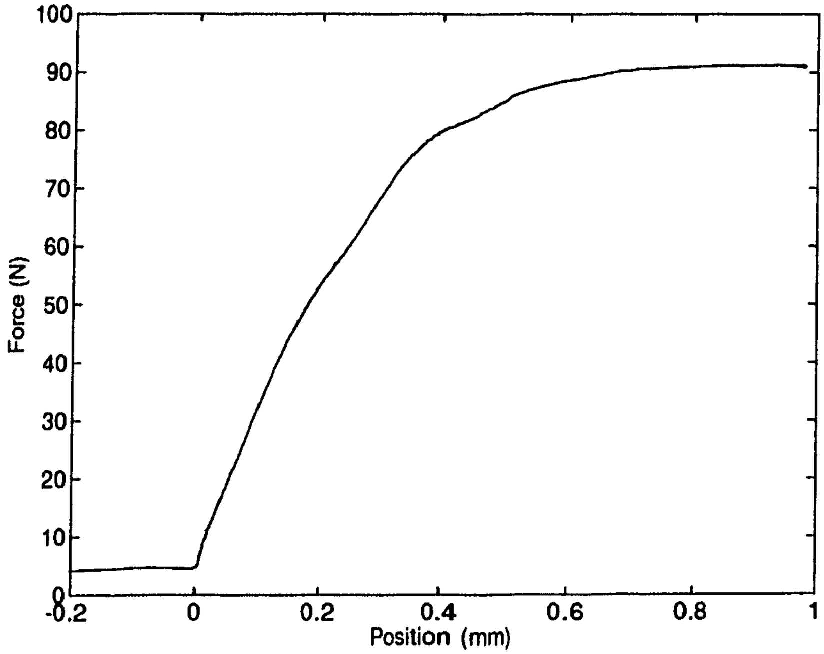

Figure 3.14: Actuator force vs. jet pipe position.

pipe major hysteresis loop data to calculate the supply and return orifice areas. The correct model parameters were obtained using the multidimensional downhill simplex method (see Press et al. [1992]). This method was used because it requires only function evaluations, not derivatives, and is able to find the minimum of a function of more than one independent variable.

The piston leakage area, A_{lpp}, could not be obtained directly but was obtained in combination with the discharge coefficient slope and offset. Referring to the model equations (2.7), (2.18) and (2.23), the identified parameters were found to be: $x_{jp,offset} = 0.099$ mm, $C_d = 0.696$, $C_{d,lpp}A_{lpp} = -0.0475\,(P_2/P_1) + 0.0971$ mm^2.

Table 3.1 lists the values for all the model parameters.

3.3.2 Dynamic Characteristics

Several open-loop sinusoidal frequency response tests were performed on the actuator with currents of varying amplitude and mean to observe the degree of nonlinearity

Element	Parameter	Value
piston/cylinder	L_{cyl}	78.0 mm
	L_p	8.0 mm
	L_s	7.0 mm
	L_{sup}	11.0 mm
	$L_{spring,0}$	69.1 mm
	D_{cyl}	15.875 mm
	k_{spring}	88.14 N/m
current driver	ω_{cd}	7050 rad/s
jet pipe	k_m	1.946 N/A
	ω_1	973.9 rad/s
	ω_2	1856.7 rad/s
	ζ_2	0.019
	D_{jp}	0.9652 mm
	$x_{jp,offset}$	0.099 mm
orifice areas	C_d	0.696
	$C_{db}A_{lpp}$	0.0971 mm^2
	$C_{dm}A_{lpp}$	−0.0475 mm^2

Table 3.1: Summary of values for model parameters.

in the system. Although not explicitly required for the identification of any model parameters, these tests qualitatively show the overall system response and provide a rough estimate for the time constant of the system.

Figure 3.15 shows the force/current frequency response for varying mean currents, with the piston at approximately the midstroke position ($x_s = 54$ mm). Figure 3.16 shows similar data for varying amplitudes. The results show a low bandwidth ranging from 0.8–2.8 Hz which increases slightly for both mean current and amplitude. This bandwidth is in agreement with the linear analysis in §4.2.2. After linearizing the actuator model about an operating point corresponding to an output force of 45 N, the system is shown to act as a first-order, low-pass filter with a corner frequency of 2.3 Hz.

From the shape of the curves it is apparent that the system is highly non-linear and acts as a low-pass filter, approaching an integrator in some sense. The physical

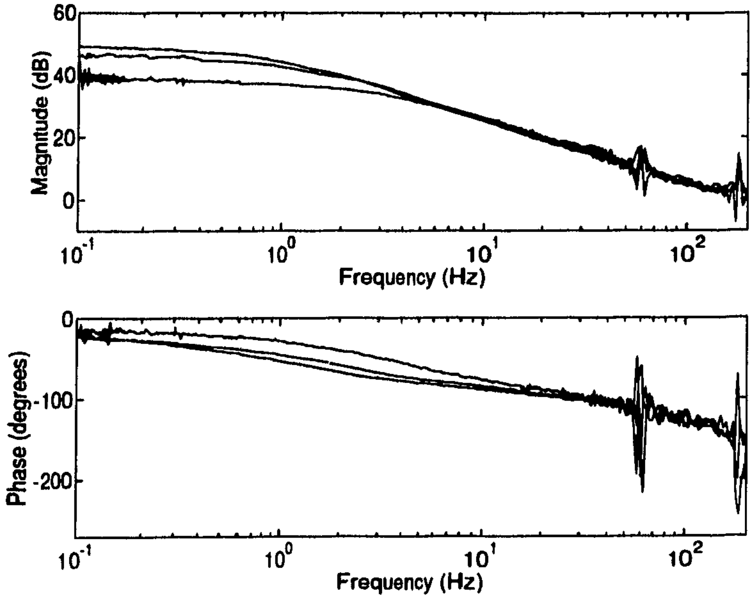

(a) Amplitude = 0.005 A

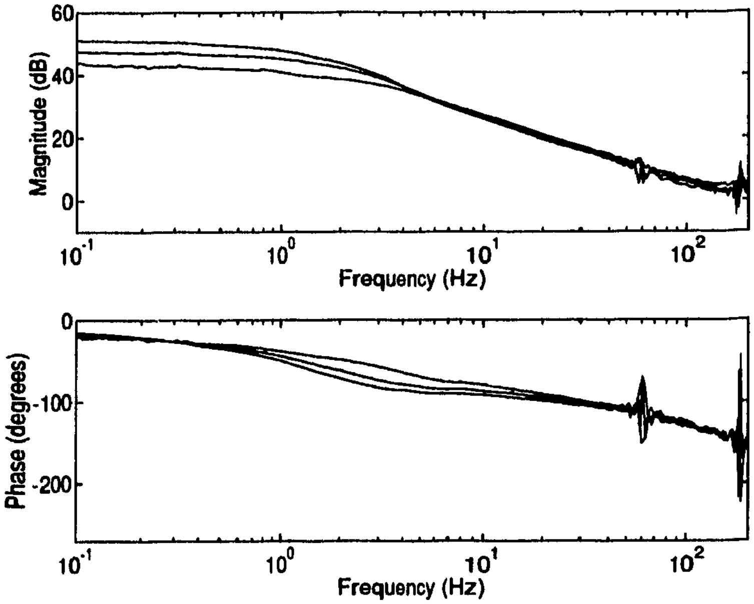

(b) Amplitude = 0.01 A

Figure 3.15: Actuator open-loop force/current frequency response for varying mean currents: $F_{act}(j\omega)/I(j\omega)$

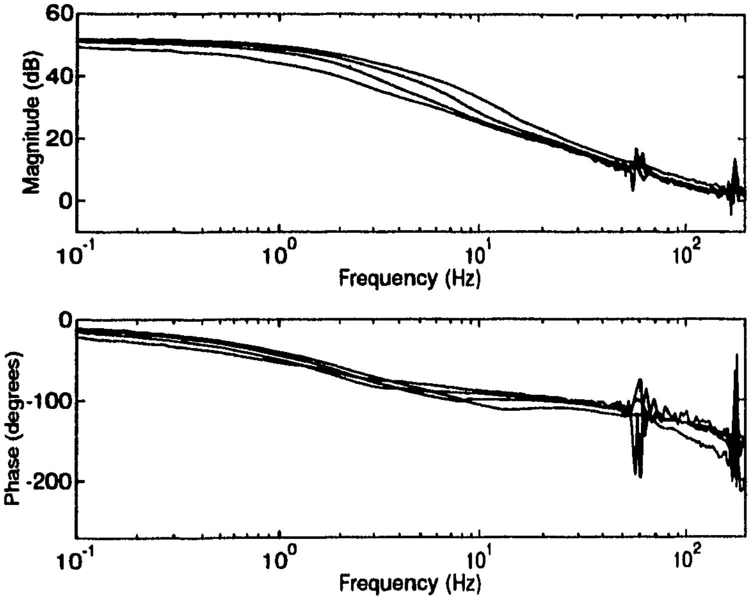

(a) Mean = 0.05 A

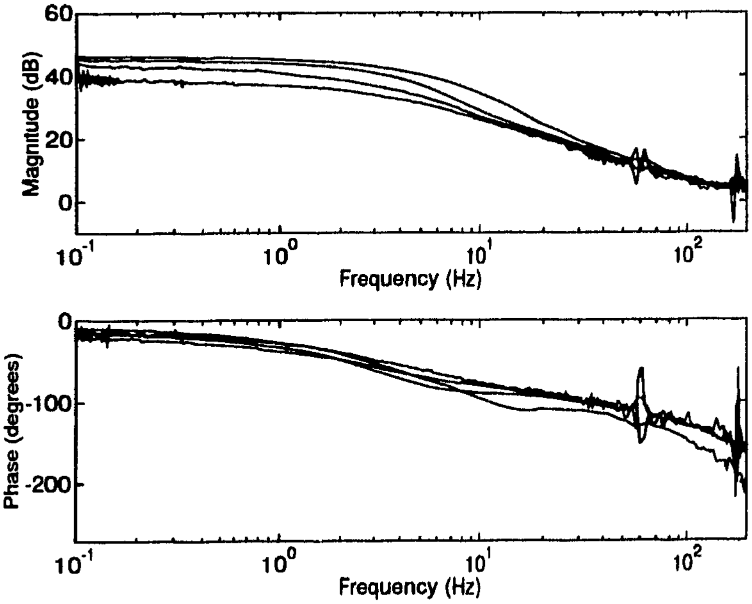

(b) Mean = 0.15 A

Figure 3.16: Actuator open-loop force/current frequency response for varying amplitude currents: $F_{act}(j\omega)/I(j\omega)$

significance of this is that the static force is almost at maximum for all positive inputs, as can be seen in Figures 3.13 and 3.14. Systems of this type require some type of feedback to linearize their response and overcome the adverse effects of hysteresis. In §4.1.1 it is shown that the bandwidth of this system can be raised as high as 80 Hz by employing a simple proportional controller.

4.1 Closed-Loop Control

The performance of the actuator and the model was examined by implementing several different digital controllers using the Condor real-time control system. The closed-loop frequency response of the actuator was tested with the aid of an HP 35665A dynamic signal analyzer which provided the input to the control system and analyzed the output. Several time-domain, force tracking experiments were performed to examine the fidelity of the model and test different control strategies. All the control loops were run at 500 Hz which is a reasonable rate for servo control.

4.1.1 Actuator Closed-Loop Frequency Response

A simple proportional feedback controller (Figure 4.2) was used to examine the closed-loop frequency response of the actuator. Figure 4.1a shows the swept sine response for three different amplitude sine waves at a mean desired force of 45 N, with the rod stopper locked at the midstroke position. Figure 4.1b shows the frequency response with the piston positioned such that the chamber 1 volume is less than chamber 2.

The vast improvement of the system under closed-loop control is immediately noticeable. At low frequencies, the system is perfectly linear. At higher frequencies, the nonlinearities in the system become apparent — the response depends on the mean and amplitude of the input. Even so, the system appears well-behaved, resembling the shape of a damped second-order system. However, the most pleasing characteristic is that the -3 dB bandwidth of the system has been pushed as high as 80 Hz for medium amplitude (5 N) inputs. For small amplitude inputs the bandwidth is substantially lower — roughly 25 Hz for a 1 N sinusoidal input. There appears to be little difference

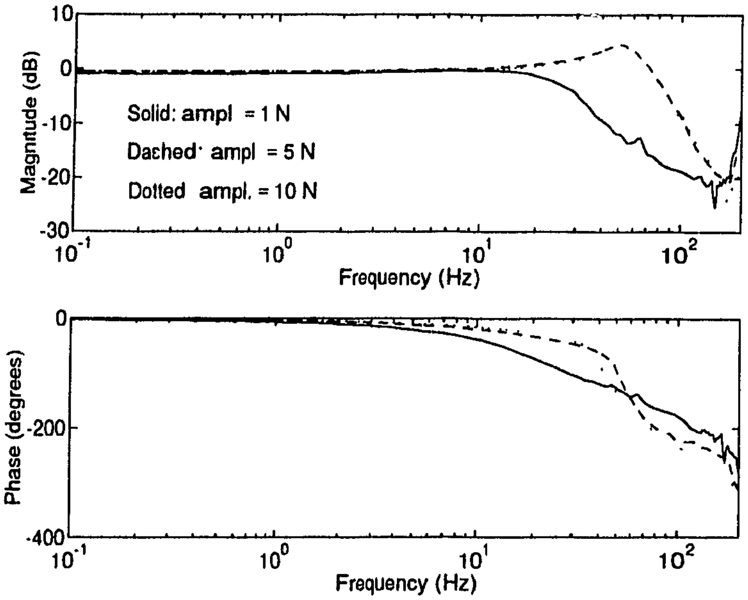

(a) $x_s = 54$ mm: Chamber 1 = Chamber 2

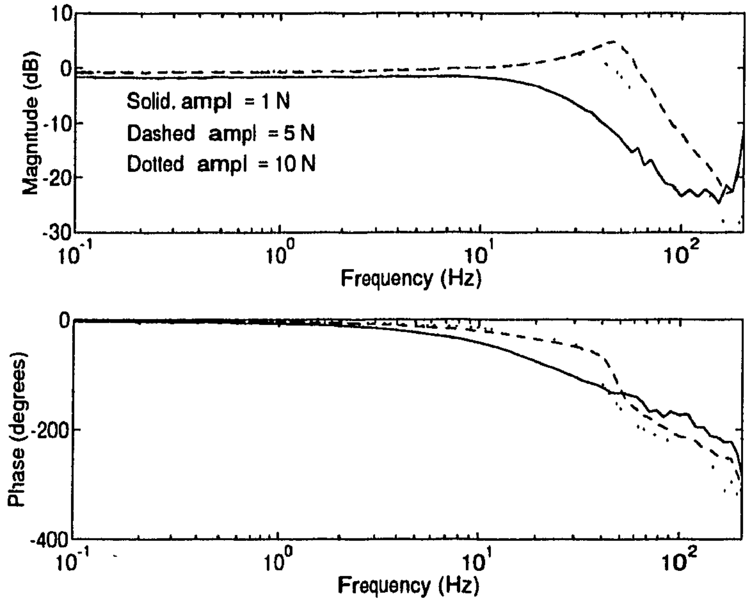

(b) $x_s = 40$ mm: Chamber 1 < Chamber 2

Figure 4.1: Actuator closed-loop frequency response: $F_a(j\omega)/F_d(j\omega)$

in dynamic response as a function of stopper position.

The difference in frequency response for the various amplitude inputs is interesting. Small amplitude inputs exhibited more damping and lower bandwidth than large amplitude inputs, which in turn exhibited more damping and lower bandwidth than medium amplitude inputs. A similar behavior was noted by Chen [1977] in the theoretical analysis of the dynamic response of a symmetric, double-sided, closed pneumatic chamber system. In that study, it was found that the resonant frequency tended to decrease with increasing amplitude.

4.1.2 Time-Domain Force Tracking

Time-domain control experiments consisted of sine and square wave tracking. The first test examined the performance of the actuator and model using a simple proportional feedback controller, and the second test used a proportional feedback plus nonlinear feedforward controller. The simulations were performed using a fourth-order Runge-Kutta (R-K) integration scheme (Press et. al. [1992]). Although other good methods do exist, this robust method is probably the most widely used. For example, Bowns and Ballard [1972] also used a fourth-order R-K method for their simulations, and Boulet et. al. [1992] used a fifth-order R-K. However, McLain et. al. [1989] chose to employ Gear's stiff integration method (see Press et. al. [1992]) which works well for very smooth functions and for sets of differential equations where there are very different scales of independent variables.

The simulation method proceeds by casting the set of differential equations governing the system dynamics into state-space form and integrating all the equations over a suitably small time period. The final values for this time period are then used as the initial values for the following integration period, and so on. "Smart" methods are able to vary the length of this time step depending on how quickly the variables are changing. The differential equations for this model are (2.1), (2.6) and (2.29). The actuator model has nonlinear elements and hence cannot be expressed in the conventional linear form, $\dot{\mathbf{x}} = \mathbf{A}\mathbf{x} + \mathbf{B}\mathbf{u}$. Therefore the state-space formulation is

$$\dot{\mathbf{x}} = \boldsymbol{\Theta}(\mathbf{x}, u) \tag{4.1}$$

where $\mathbf{x} = [\ i \quad \ddot{x}_{jp} \quad \dot{x}_{jp} \quad x_{jp} \quad P_1 \quad P_2\ ]^T$ is the vector of state variables, u is the D/A input voltage, and $\boldsymbol{\Theta}$ is the set of state equations. All the other relations, including the output actuator force, are static relations and hence are obtained at any time from the corresponding state variables.

Figures 4.4–4.6 show experimental and theoretical results for the tracking of various frequency sine waves using the proportional feedback controller (Figure 4.2). The correlation between the model and experimental data is very good, although there is a significant offset between the actual and desired force levels. Raising the feedback gain can reduce the offset but higher gain can also lead to instability. Nonetheless, the performance of the simple proportional controller is very good.

To reduce the offset without increasing the gain, a feedback/feedforward controller (Figure 4.3) was implemented where the feedforward term was equal to the inverse of the static actuator force/current relationship. That is, if the midpoint line of the force/current data in Figure 3.13 is represented by $F_a = f(\bar{i})$, then the nonlinear feedforward term is $\bar{i} = f^{-1}(F_d)$. Therefore, the proportional feedback/feedforward controller output is

$$i = k_p(F_d - F_a) + f^{-1}(F_d) \tag{4.2}$$

As shown in Figures 4.7–4.9 for the tracking of various frequency square waves, this controller proved to be very effective in eliminating any offset between the desired and actual force. Figures 4.10 and 4.11 show a direct comparison between the proportional feedback and feedback/feedforward controllers.

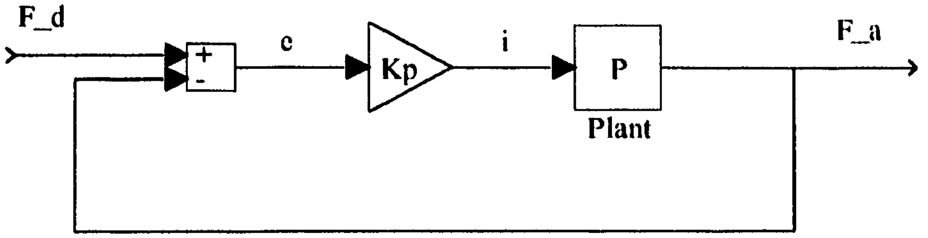

Figure 4.2: Proportional feedback controller. F_d and F_a are desired and actual actuator forces respectively.

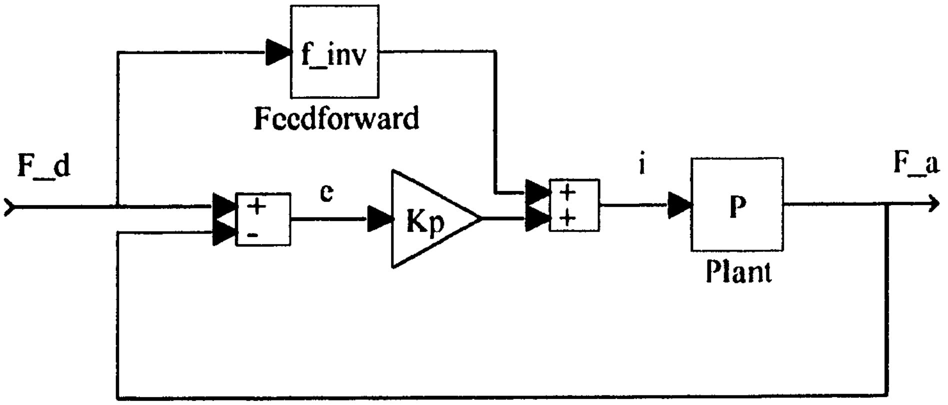

Figure 4.3: Feedback/feedforward controller. F_d and F_a are desired and actual actuator forces respectively.

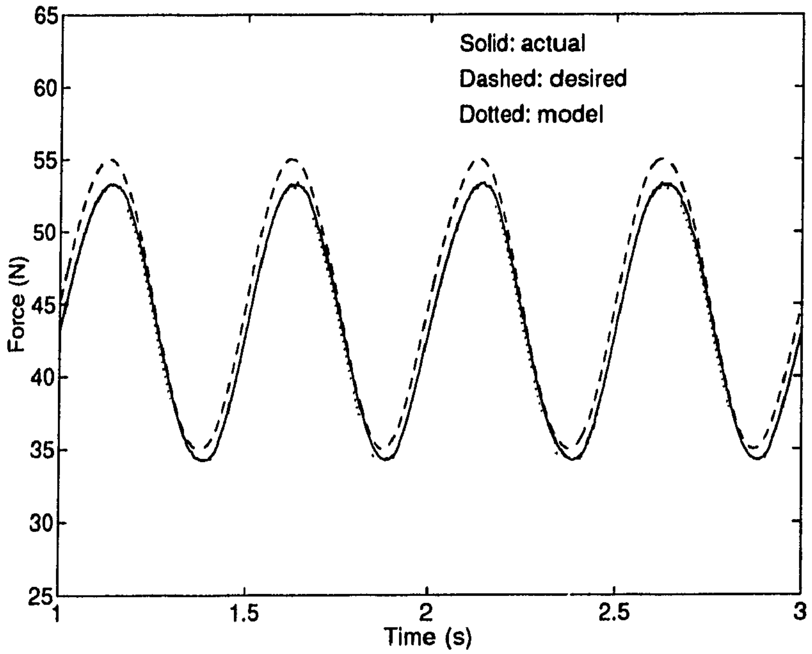

Figure 4.4: Force tracking using proportional feedback controller: 2 Hz sine wave.

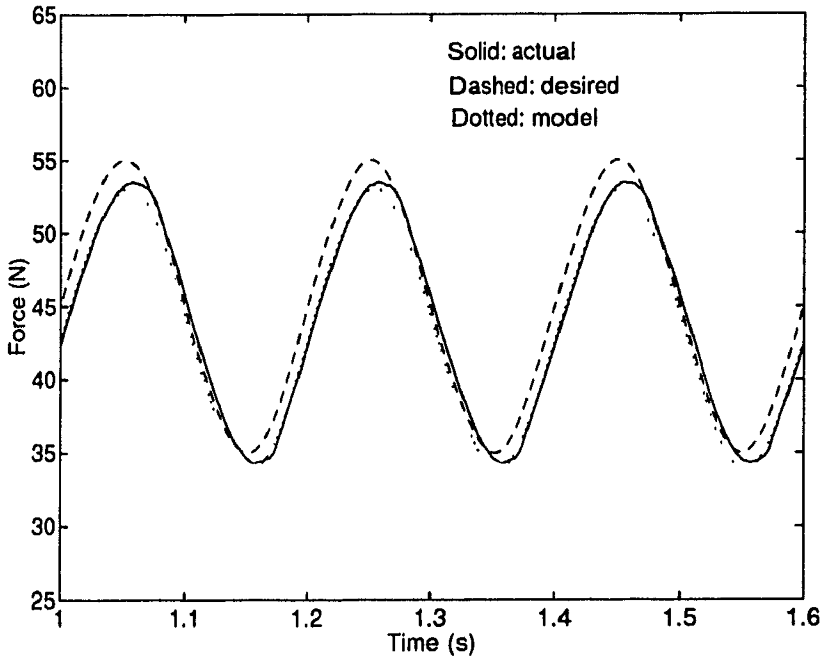

Figure 4.5: Force tracking using proportional feedback controller: 5 Hz sine wave.

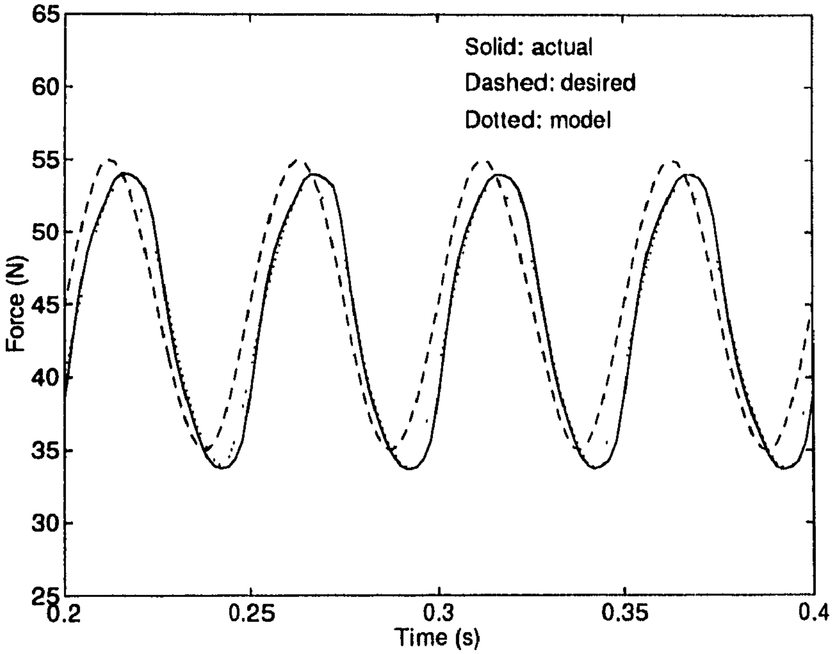

Figure 4.6: Force tracking using proportional feedback controller: 20 Hz sine wave.

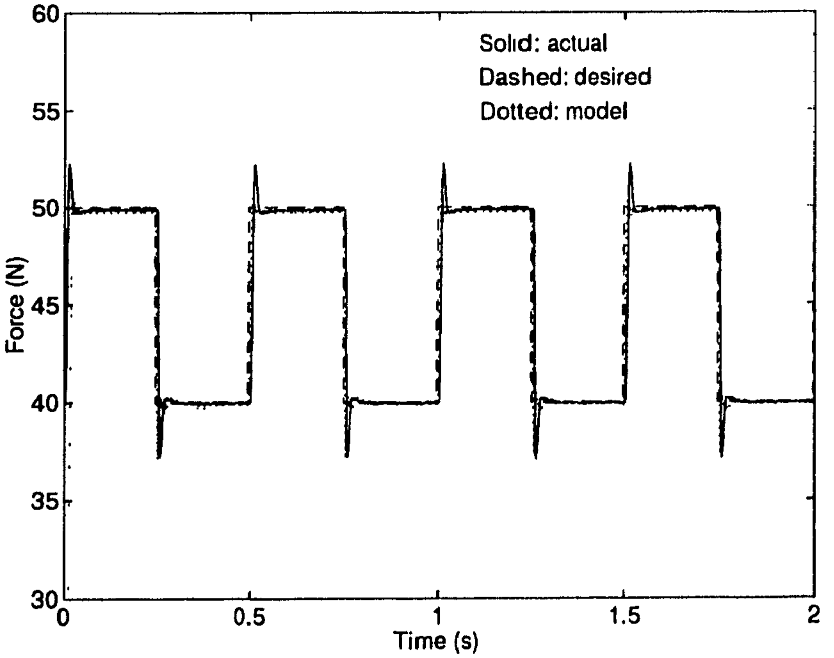

Figure 4.7: Force tracking using feedback/feedforward controller: 2 Hz square wave.

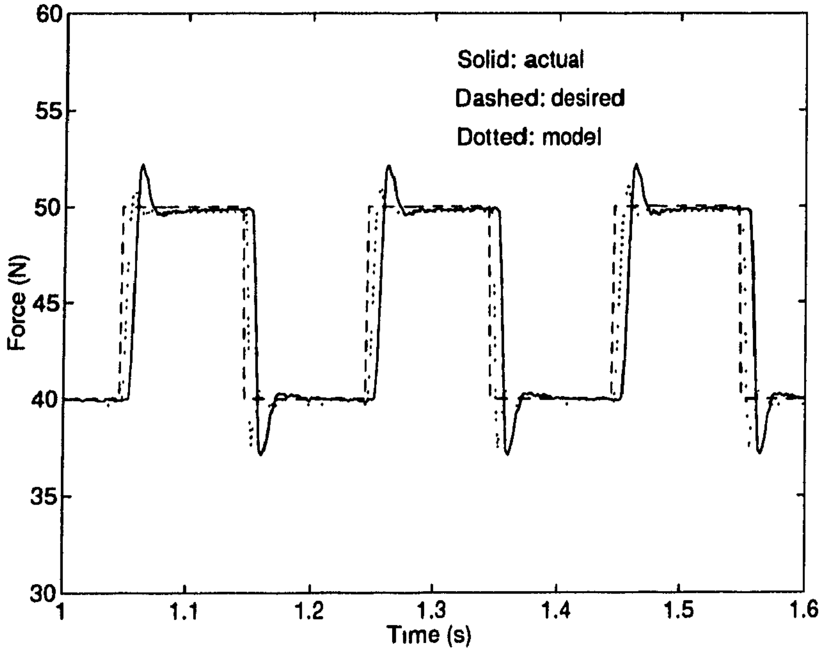

Figure 4.8: Force tracking using feedback/feedforward controller: 5 Hz square wave.

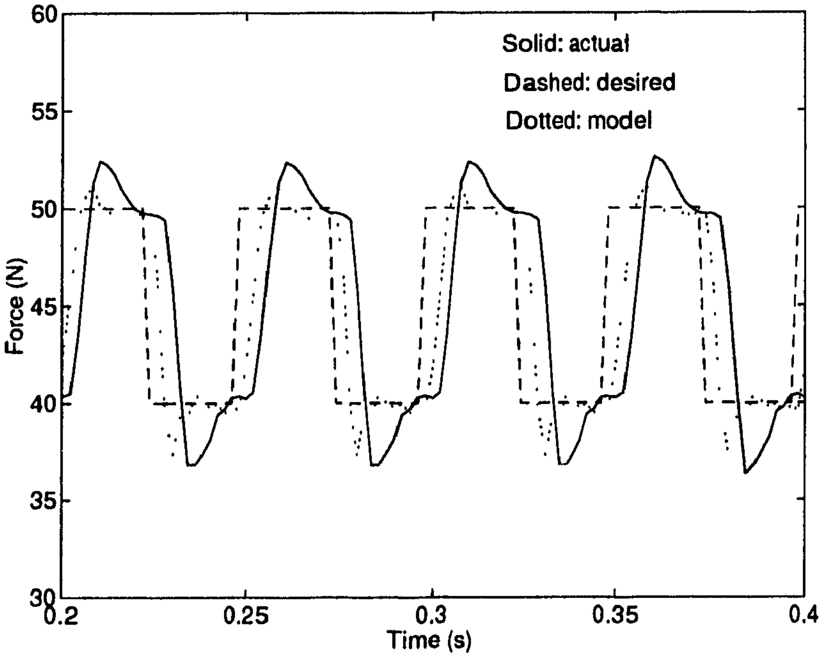

Figure 4.9: Force tracking using feedback/feedforward controller: 20 Hz square wave.

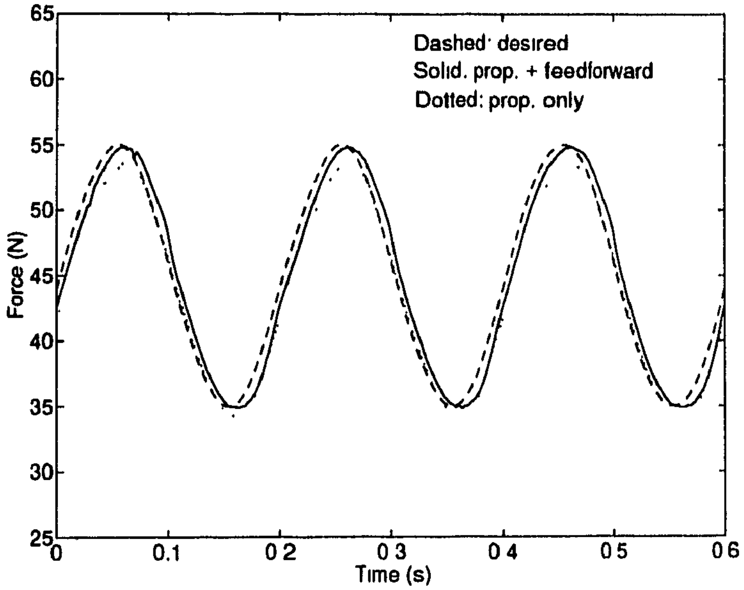

Figure 4.10: Comparison between proportional feedback and feedback/feedforward controllers for a 5 Hz sine wave.

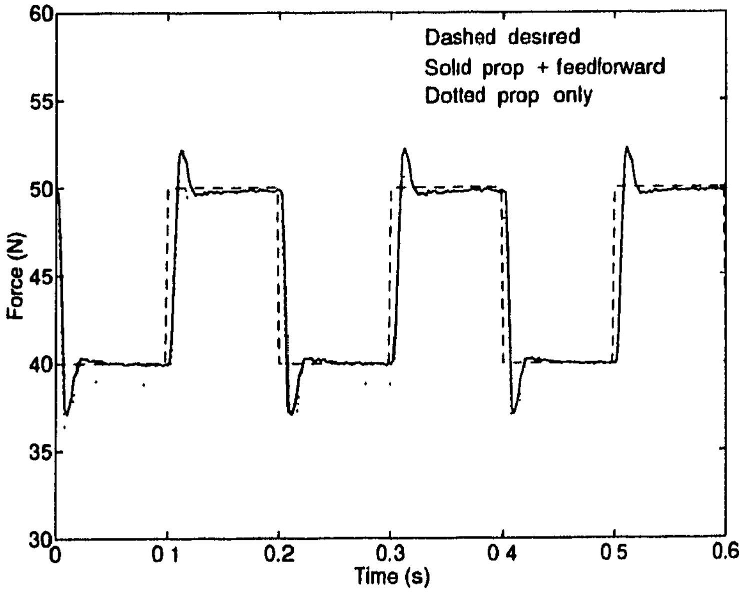

Figure 4.11: Comparison between proportional feedback and feedback/feedforward controllers for a 5 Hz square wave.

4.2 Linear Analysis

4.2.1 Actuator Closed-Loop Frequency Response

A linear analysis was performed to explain the vast improvement in bandwidth using the proportional feedback controller (Figure 4.2). If the plant dynamics are approximated by a first-order linear model, as open-loop frequency response tests and a linear analysis (see §4.2.2) have suggested, the closed-loop response of the system using a feedback gain of k_p can be determined as follows:

$$\begin{aligned} \text{plant dynamics:} \quad & P(s) = \frac{F_a(s)}{I(s)} = k\left(\frac{a}{s+a}\right) \\ \text{controller:} \quad & i = k_p e = k_p(F_d - F_a) \\ \text{system dynamics:} \quad & \frac{F_a(s)}{F_d(s)} = \frac{k_p k a}{s + a + k_p k a} \end{aligned}$$

where F_d is the desired force, F_a is the actual force, and a is the plant open-loop bandwidth.

Note that the system bandwidth has been raised from a to $a + k_p k a$. Note also that the steady state gain is $k_p k a/(a + k_p k a)$, which is marginally less than unity. Systems with a large value of k can benefit enormously from even small feedback gains. A quick check of Figure 3.13 or 3.15 reveals that the system has a k value of ≈ 550 N/A, or 55 dB, which is very large indeed.

The linear analysis in §4.2.2 shows that the theoretical open-loop system bandwidth, a, is 2.3 Hz for small perturbations about a 45 N output force operating point. Using this value, and the value of the feedback gain which was used in the closed-loop force control experiments, $k_p = 0.044$ A/N, the theoretical closed-loop bandwidth for the linear system, ω_{cl}, can be computed:

$$\begin{aligned} \omega_{cl} &= a + k_p k a \\ &= 13.8 + (0.044)(550)(13.8) = 347.8 \text{ rad/s} \approx 55 \text{ Hz} \end{aligned}$$

This value agrees well with the experimentally observed bandwidth in Figure 4.1. Although the theoretical closed-loop system is stable for all positive feedback gains, in practice sensor noise and unmodelled dynamics limit the size of the gain that can be used before instability occurs. For the UMDH, force feedback information would be affected by the dynamics and friction of the tendon transmission system since the force sensors are located at the wrist (i.e. non-colocated).

4.2.2 Linearized Model

To gain some qualitative insight into the parameters that influence the response of the actuator and model, a linear analysis of the jet pipe and fluid flow equations was performed for small perturbations about a nominal set operating conditions. The following derivation assumes:

1. Positive input current (a_{s1} and $a_{r2} > 0$, a_{s2} and $a_{r1} = 0$).
2. Non-choked flow through orifice 1.
3. Non-choked flow past the piston.
4. Choked flow through orifice 2.
5. Constant temperature.
6. Constant chamber volumes (i.e. stationary piston).

The assumption of whether the flow is choked or non-choked is not as crucial as it might appear since the fluid flow is continuous as it changes from subsonic to sonic. In any case, the assumptions were based on conditions observed during simulation using the complete nonlinear dynamic model.

The constants, c_i and k_i, used below are defined in Appendix A, and are all positive. Nominal conditions are denoted by the subscript "0". Changes from the nominal conditions are indicated by Δ.

• Current Driver

The current driver dynamics (2.1) can be expressed as

$$\dot{i} = g_a(i, \bar{i}) \tag{4.3}$$

Using (2.3), which relates the static current, $\bar{i}$, to the D/A voltage, $v_{D/A}$, the above equation can be linearized as

$$\begin{aligned} \Delta\dot{i} &= \frac{\partial g_a}{\partial i}\Delta i + \frac{\partial g_a}{\partial \bar{i}} \cdot \frac{\partial \bar{i}}{\partial v_{D/A}}\Delta v_{D/A} && (4.4) \\ &= -c_0\Delta i + c_1\Delta v_{D/A} && (4.5) \end{aligned}$$

• Jet Pipe

The jet pipe dynamics (2.6) can be expressed as

$$x^{(3)}{}_{jp} = g_b(\ddot{x}_{jp}, \dot{x}_{jp}, x_{jp}, \bar{x}_{jp}) \tag{4.6}$$

Using (2.4) and (2.5), the above equation can be linearized as

$$\begin{aligned} \Delta x^{(3)}{}_{jp} &= \frac{\partial g_b}{\partial \ddot{x}_{jp}}\Delta\ddot{x}_{jp} + \frac{\partial g_b}{\partial \dot{x}_{jp}}\Delta\dot{x}_{jp} + \frac{\partial g_b}{\partial x_{jp}}\Delta x_{jp} + \frac{\partial g_b}{\partial \bar{x}_{jp}} \cdot \frac{\partial \bar{x}_{jp}}{\partial F_{jp}} \cdot \frac{\partial F_{jp}}{\partial i}\Delta i && (4.7) \\ &= -c_2\Delta\ddot{x}_{jp} - c_3\Delta\dot{x}_{jp} - c_4\Delta x_{jp} + c_5\Delta i && (4.8) \end{aligned}$$

• Flow Equations

From (2.18), (2.24) and (2.25):

$$\begin{aligned} \dot{m}_{s1} &= f_a(a_{s1}, P_1) && (4.9) \\ \dot{m}_{r2} &= f_b(a_{r2}, P_2) && (4.10) \\ \dot{m}_{lpp} &= f_c(P_1, P_2) && (4.11) \end{aligned}$$

Assuming all variables undergo small variations from their initial values, these equations can be written in linearized form:

$$\Delta\dot{m}_{s1} = \frac{\partial f_a}{\partial a_{s1}} \cdot \frac{\partial a_{s1}}{\partial x_{jp}} \Delta x_{jp} + \frac{\partial f_a}{\partial P_1} \Delta P_1 \tag{4.12}$$

$$= k_0 \Delta x_{jp} - k_1 \Delta P_1 \tag{4.13}$$

$$\Delta\dot{m}_{r2} = \frac{\partial f_b}{\partial a_{r2}} \cdot \frac{\partial a_{r2}}{\partial x_{jp}} \Delta x_{jp} + \frac{\partial f_b}{\partial P_2} \Delta P_2 \tag{4.14}$$

$$= k_2 \Delta x_{jp} + k_3 \Delta P_2 \tag{4.15}$$

$$\Delta\dot{m}_{lpp} = \frac{\partial f_c}{\partial P_1} \Delta P_1 + \frac{\partial f_b}{\partial P_2} \Delta P_2 \tag{4.16}$$

$$= k_4 \Delta P_1 - k_5 \Delta P_2 \tag{4.17}$$

$$\Delta\dot{m}_1 = \Delta\dot{m}_{s1} - \Delta\dot{m}_{lpp} \tag{4.18}$$

$$\Delta\dot{m}_2 = \Delta\dot{m}_{lpp} - \Delta\dot{m}_{r2} \tag{4.19}$$

From (2.26), and noting $\rho_i/\rho_{i0} = P_i/P_{i0}$:

$$Q_1 = f_d(\dot{m}_1, P_1) \tag{4.20}$$

$$Q_2 = f_e(\dot{m}_2, P_2) \tag{4.21}$$

Linearizing (4.20) and (4.21) gives

$$\Delta Q_1 = \frac{\partial f_d}{\partial \dot{m}_1} \Delta\dot{m}_1 + \frac{\partial f_d}{\partial P_1} \Delta P_1 \tag{4.22}$$

$$= k_6 \Delta\dot{m}_1 \tag{4.23}$$

$$\Delta Q_2 = \frac{\partial f_e}{\partial \dot{m}_2} \Delta\dot{m}_2 + \frac{\partial f_e}{\partial P_2} \Delta P_2 \tag{4.24}$$

$$= k_7 \Delta\dot{m}_2 \tag{4.25}$$

From (2.29):

$$\dot{P}_1 = f_f(P_1, Q_1) \tag{4.26}$$

$$\dot{P}_2 = f_g(P_2, Q_2) \tag{4.27}$$

Linearizing (4.26) and (4.27) gives

$$\begin{aligned}
\Delta\dot{P}_1 &= \frac{\partial f_f}{\partial P_1}\Delta P_1 + \frac{\partial f_f}{\partial Q_1}\Delta Q_1 && (4.28)\\
&= k_8 \Delta Q_1 && (4.29)\\
\Delta\dot{P}_2 &= \frac{\partial f_g}{\partial P_2}\Delta P_2 + \frac{\partial f_g}{\partial Q_2}\Delta Q_2 && (4.30)\\
&= k_9 \Delta Q_2 && (4.31)
\end{aligned}$$

Finally, combining (4.5), (4.8), (4.18), (4.19), (4.23), (4.25), (4.29) and (4.31) and rearranging into linear state-space form yields the linearized model for the actuator:

$$\begin{aligned}
\dot{\mathbf{x}} &= \mathbf{A}\mathbf{x} + \mathbf{B}u\\
y &= \mathbf{C}\mathbf{x}
\end{aligned}$$

$$\frac{d}{dt}\begin{bmatrix} \Delta i \\ \Delta\ddot{x}_{jp} \\ \Delta\dot{x}_{jp} \\ \Delta x_{jp} \\ \Delta P_1 \\ \Delta P_2 \end{bmatrix} = \begin{bmatrix} -c_0 & 0 & 0 & 0 & 0 & 0 \\ c_5 & -c_2 & -c_3 & -c_4 & 0 & 0 \\ 0 & 1 & 0 & 0 & 0 & 0 \\ 0 & 0 & 1 & 0 & 0 & 0 \\ 0 & 0 & 0 & k_{14} & -k_{10} & k_{11} \\ 0 & 0 & 0 & -k_{15} & k_{12} & -k_{13} \end{bmatrix} \begin{bmatrix} \Delta i \\ \Delta\ddot{x}_{jp} \\ \Delta\dot{x}_{jp} \\ \Delta x_{jp} \\ \Delta P_1 \\ \Delta P_2 \end{bmatrix} + \begin{bmatrix} c_1 \\ 0 \\ 0 \\ 0 \\ 0 \\ 0 \end{bmatrix} \Delta v_{D/A} \tag{4.32}$$

$$\Delta F_{act} = \begin{bmatrix} 0 & 0 & 0 & 0 & A_p & -A_p \end{bmatrix} \begin{bmatrix} \Delta i \\ \Delta\ddot{x}_{jp} \\ \Delta\dot{x}_{jp} \\ \Delta x_{jp} \\ \Delta P_1 \\ \Delta P_2 \end{bmatrix} \tag{4.33}$$

The poles and zeros of the linearized system for operating conditions corresponding to an actuator output force of 45 N and stopper position of 54 mm are shown in Table 4.1. The single zero at 1.1 Hz contributed by the fluid dynamics is located very close

Element	Zero	Pole
current driver		-7049.7
jet pipe		-973.9 $-35.3 \pm 1856.3j$
fluid dynamics	-7.1	-5.0 -14.5

Table 4.1: Poles and zeros (rad/s) of linearized actuator model for actuator force of 45 N with piston at midstroke position.

to the pole at 0.8 Hz and therefore effectively cancels this term out. Although this model is sixth-order, the remaining pole due to the fluid dynamics is at a very low frequency (2.3 Hz) and hence dictates the overall system response. Therefore, the actuator, at this operating point, tends to behave like a first-order, low-pass system with a corner frequency of 2.3 Hz. This frequency compares well with the observed range of 0.8–2.8 Hz described in §3.3.2. Since there is a large amount of hysteresis in the actuator force/current relationship, there is no single current which corresponds to a given actuator output force. Therefore comparison between the experimental, open-loop, force/current frequency response and the theoretical response which excludes hysteresis is only qualitative.

To investigate the effect of the operating point of the linearized model on the open-loop bandwidth, the bandwidth was obtained as a function of the rod stopper position, x_s, at several different actuator output forces, F_{act} (Figure 4.12). The results show that the open-loop bandwidth is inversely proportional to the chamber 1 volume and increases with actuator output force. The latter behavior was observed during experimental frequency response tests performed on the actuator (see §3.3.2).

The information obtained by linearizing the model for a variety of operating points can be used by the control system to aid in the selection of feedback gains, and in the analysis of stability. For example, a function could be derived relating stopper position and actuator force to open-loop bandwidth. Since the piston rods are directly

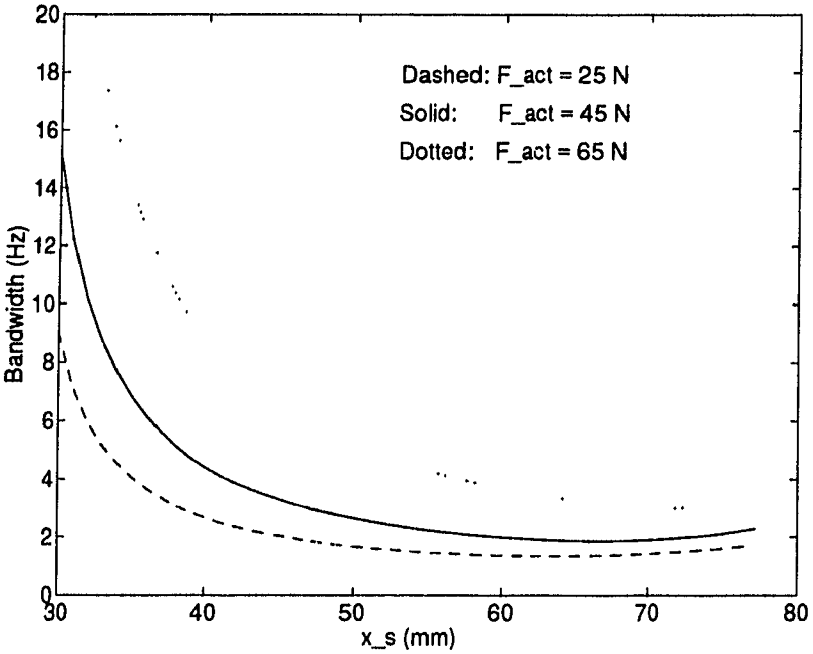

Figure 4.12: Effect of operating point on actuator open-loop bandwidth.

connected to the robot finger joint via the tendons, the stopper position could easily be calculated using joint angle information. Tendon tension information provided by the force sensors provides a reasonably accurate estimate of actuator force. These parameters could be monitored by the control system in real-time and feedback gains dynamically adjusted to obtain a constant level of performance regardless of the operation.

4.2.3 Comparison with Nonlinear Actuator Model

The performance of the linearized model was examined by comparing force-control simulations using the linearized and nonlinear models with experimental data. A set of nominal conditions for the linearized model was selected corresponding to the same experimental conditions: $F_{act} = 45$ N, $x_s = 54$ mm.

Figures 4.13 and 4.14 show comparisons between simulations using the linearized and nonlinear models for closed-loop, proportional feedback control. The results

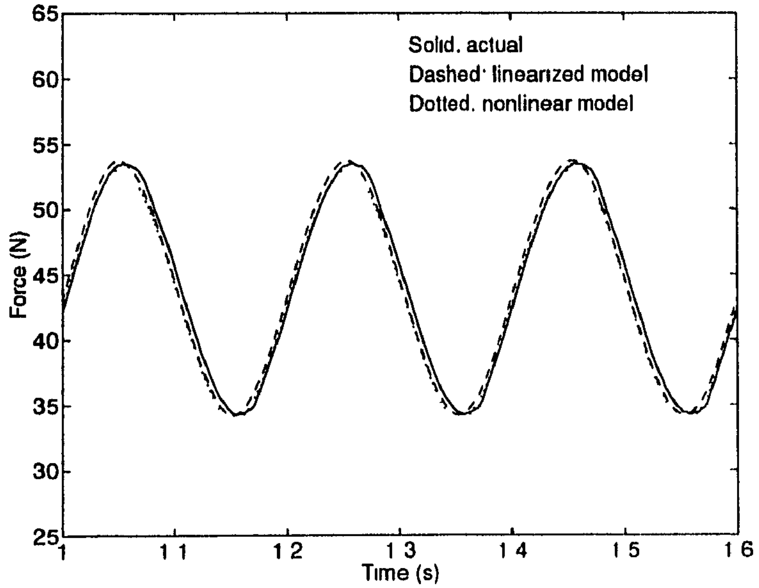

(a) Comparison with experimental data

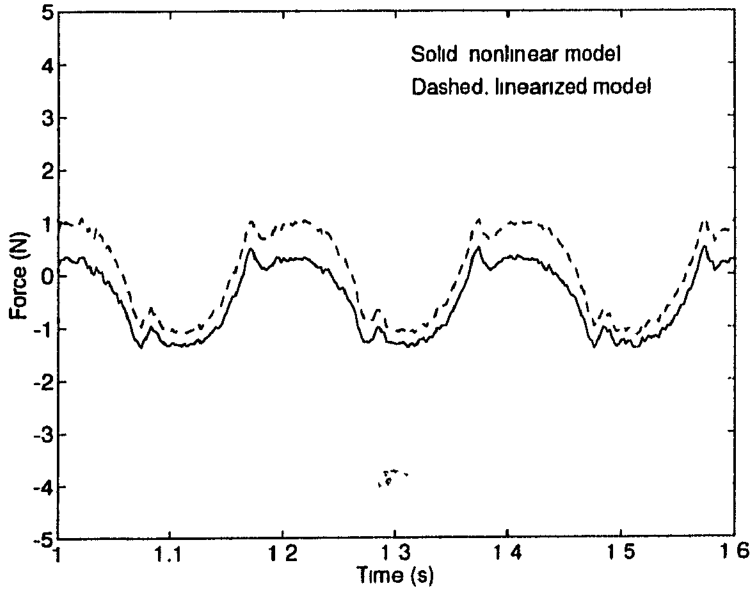

(b) Error between model and experimental data

Figure 4.13: Comparison between linearized and nonlinear model for tracking 5 Hz sine wave: Proportional controller.

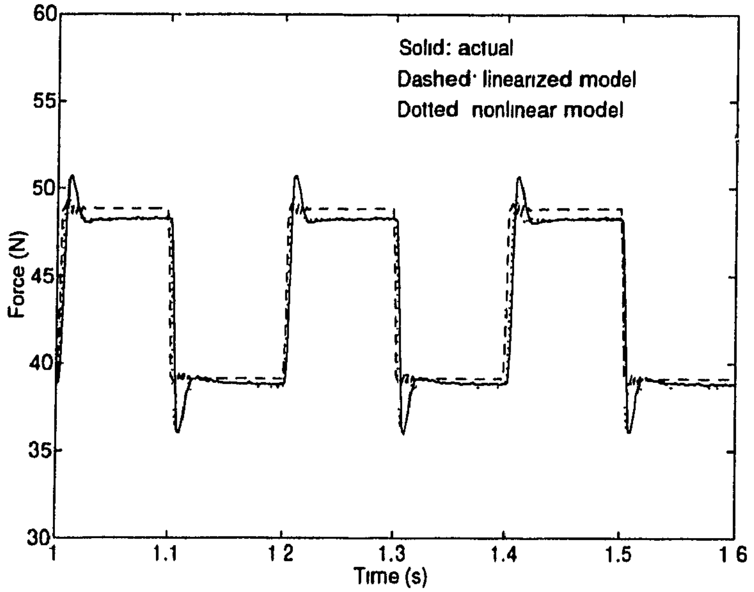

(a) Comparison with experimental data

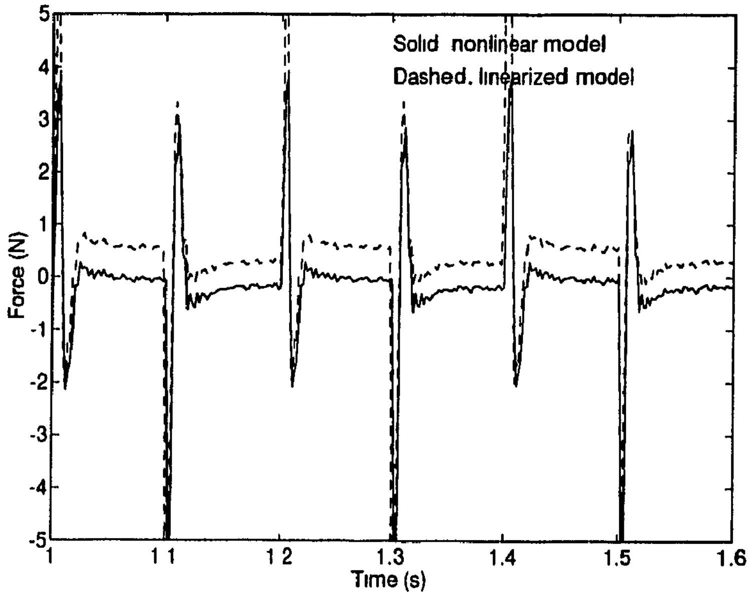

(b) Error between model and experimental data

Figure 4.14: Comparison between linearized and nonlinear model for tracking 5 Hz square wave: Proportional controller.

show a high degree of correlation between the two models and the experimental data, although there is a slight offset with the linearized model in the square wave test. Nonetheless, the linearized model is shown to perform as well as the nonlinear model at this operating point.

However, the linearized model is only valid for small perturbations about the given operating point, and therefore can expected to perform poorly for very different conditions. For instance, the orifice area functions and jet pipe saturation regions introduce nonlinearities which are not adequately accounted for with a single operating point. For instance, linearizing the model for a variety of operating points (Figure 4.12) shows that the open-loop bandwidth varies significantly with stopper position and actuator force. To overcome this fundamental problem with linearized models, time-varying models can be used to essentially move the operating point as the operating conditions change. Of course this requires the existence of a nonlinear model to begin with, a fact that further reinforces the value of a detailed nonlinear model.

5. Conclusions

5.1 Summary

This thesis has presented the results of an analytical and experimental investigation of a suspension-type, jet pipe valve electropneumatic actuator designed for use in the Utah/MIT Dextrous Hand. Actuator capabilities play a key role in overall dextrous hand performance and as such, detailed knowledge of actuator properties and limitations can greatly aid in the design of control systems to improve performance.

The research was divided into the following sections:

1. Formulation of a complete nonlinear mathematical model of the actuator actuator including detailed representation of the current driver, jet pipe element, orifice areas and fluid flows.
2. Identification of model parameters.
3. Characterization and simulation of hysteretic elements.
4. Experimental and theoretical closed-loop force control.
5. Linearized analysis of actuator response and comparison with nonlinear model.

The mathematical model developed in this thesis features a number of nonlinear elements which proved to be quite difficult to characterize. The jet pipe and coil were each shown to have a fair amount of hysteresis, although this effect could not be modelled successfully using the method proposed by Frame et al. [1982]. The constitutive equations for flow through orifices are inherently nonlinear, as are the orifice areas as a function of jet pipe position, thus adding to the complexity of the model.

The uncertainty of jet pipe position during dynamic tests and the existence of many nonlinearities in the system precluded the use of linear identification techniques. Instead, the experimental jet pipe position major hysteresis loop was used in conjunction with the actuator output force major loop to synchronize the input and output for the model. In this manner, the required model parameters were able to be identified with only static measurements using the multidimensional downhill simplex method.

Investigation of the jet pipe element revealed a significant amount of hysteresis in the position/current relationship (≈ 8 %). Dynamic testing of the jet pipe showed that the system is well approximated up to 700 Hz by a linear third-order system. The pipe has little damping ($\zeta = 0.019$) and a high natural frequency ($\omega_n = 295.5$ Hz) which results in a very fast-acting system. The system response also includes a low-pass filter element with a corner frequency of 155 Hz. For comparison, a model of the two-stage, version I valve given in Jacobsen et al. [1984a] represented the jet pipe by a first-order system with a corner frequency of 250 Hz.

Open-loop force/current frequency response tests of the actuator confirmed that the system is highly nonlinear. With the piston locked at the midstroke position, the open-loop bandwidth was roughly 0.8 2.8 Hz and increased slightly with mean actuator force. The overall system response is dominated by the fluid dynamics and approaches that of an integrator in some sense – the static output force is almost at maximum for all positive inputs.

5.1.1 Control

Closed-loop. swept sine frequency response experiments showed that the bandwidth could be raised as high as 80 Hz for medium amplitude inputs. However, the frequency response for small amplitude inputs was observed to much lower at roughly 25 Hz. Proportional feedback successfully linearized the system at low frequencies, although the system response was still visibly nonlinear at higher frequencies. Tests performed by Jacobsen et al. [1984a] on the two-stage version of the valve using a linearizing servo amplifier showed a bandwidth of approximately 20 Hz for the stationary load case, although the amplitude of the input signal is not specified.

Time-domain, force control experiments consisted of tracking various amplitude and frequency waveforms. A feedforward term was shown to aid the proportional feedback controller in eliminating any offset between the actual and desired force levels. The nonlinear model was shown to predict the system response remarkably well.

The high level of performance observed using the proportional and proportional-plus-feedforward controllers proves that these actuators are well designed for their application. Performance is expected to degrade slightly during normal operation of the hand because of the non-colocated force sensors and intervening transmission dynamics which affect the force feedback information. In fact, a study of the transmission system by Nahvi et al. [1994] concluded that the friction of the routing pulleys is not negligible and should be considered in the control of the UMDH.

5.1.2 Linear Analysis

A linear model of the actuator was developed which can easily be adapted for any operating point. Theoretical analysis showed that the system open-loop bandwidth is inversely proportional to the chamber 1 volume and increases with actuator force. The theoretical open-loop system bandwidth compared well with experimental results which reinforces the validity of the model.

Comparison with the nonlinear model showed the linearized model to perform equally well for closed-loop force control when the appropriate operating point was selected. This fact reinforces the value of the nonlinear model and suggests that a time-varying linear model could perhaps be used for control purposes.

5.2 Future Work

Further work related to the actuator model might involve refinement of the fluid flow portion of the model to explicitly account for the clearance between the jet pipe tip and the receiver plate. Furthermore, all actuator testing was performed with the piston held stationary. Although the model works well under this condition, dynamic testing would permit the study of friction inside the cylinder and possible rate limiting due to finite flow from the valve.

The model derived in this thesis is for the single-cylinder actuator design and requires some adaptation for the double-cylinder design, although the valve portion of the model is the same. Since it is not practical to instrument every actuator to measure the jet pipe position, the jet pipe parameters given here should probably be used for all the actuators. Identification of the remaining parameters (discharge coefficients and receiver plate offset) could be obtained using the force/current major hysteresis loops as measured by the force sensors at the wrist, assuming the friction in the transmission system is negligible or can be accounted for. As outlined in §3.3.1, identification requires only the jet pipe and actuator major hysteresis loops.

Implementation of model-based control on the Utah/MIT Dextrous Hand necessitates the modelling of all the subsystems including: actuators, tendon transmission system, finger kinematic and inertial parameters, and sensors. Research is currently underway to characterize the tendon transmission system, including the effects of tendon dynamics and pulley friction, with future plans directed towards kinematic calibration. Model-based control is a large and complex issue and should be investigated in a systematic and careful manner.

Other control strategies could also be investigated. Xu et al. [1993] (see also Xu et al. [1994]) present a non-model-based, nonlinear PD controller which actively raises the damping and stiffness when the motion is in an unfavorable direction. This controller, which is related to the original analog controller designed for the UMDH (Jacobsen et al. [1984b]), is easy to implement and would permit very fast servo rates.

A. Constants for Linearized Actuator Model

Below are the constants for the linearized model in §4.2.2. The trailing subscript "0" on system parameters represents nominal operating point conditions. The partial derivatives are evaluated at nominal conditions.

- **Current Driver and Jet Pipe**

$$\frac{\partial \bar{x}_{jp}}{\partial F_{JP}} = \text{slope of jet pipe position/force midpoint line (Figure 3.5)}$$

$$\begin{aligned} c_0 &= \omega_{cd} & c_3 &= 2\zeta_2\omega_1\omega_2 + {\omega_2}^2 \\ c_1 &= \omega_{cd} k_{cd} & c_4 &= \omega_1{\omega_2}^2 \\ c_2 &= 2\zeta_2\omega_2 + \omega_1 & c_5 &= \omega_1{\omega_2}^2 k_m \cdot \frac{\partial \bar{x}_{JP}}{\partial F_{JP}} \end{aligned}$$

- **Flow Equations**

$$\begin{aligned} \frac{\partial f_2}{\partial P_1} &= \frac{1}{2P_1}\left[\left(\frac{P_1}{P_s}\right)^{2/\gamma} - \left(\frac{P_1}{P_s}\right)^{(\gamma+1)/\gamma}\right]^{-1/2} \left[\frac{2}{\gamma}\left(\frac{P_1}{P_s}\right)^{2/\gamma} - \frac{\gamma+1}{\gamma}\left(\frac{P_1}{P_s}\right)^{(\gamma+1)/\gamma}\right] \\ \frac{\partial a_{s1}}{\partial x_{jp}} &= 2\sqrt{r^2 - a^2} \\ \frac{\partial a_{r2}}{\partial x_{jp}} &= 2u\sqrt{r^2 - u^2}\left(\frac{1}{u} - \frac{1}{\sqrt{8r^2 - u^2}}\right)\left[\left(\frac{2r}{x_{jp} + 2r}\right)^2 + \frac{1}{2}\right] \end{aligned}$$

where $r = R_{jp}$, $a = R_{jp} - x_{JP}/2$, $u = {D_{jp}}^2/c - c/2$, and $c = x_{JP} + D_{jp}$.

$$\begin{aligned}
k_0 &= \frac{C_d P_s C_2 f_{20}}{\sqrt{T_0}} \cdot \frac{\partial a_{s1}}{\partial x_{jp}} \\
k_1 &= -\frac{C_d a_{s10} P_s C_2}{\sqrt{T_0}} \cdot \frac{\partial f_2}{\partial P_1} \\
k_2 &= \frac{C_d P_{10} C_1}{\sqrt{T_0}} \cdot \frac{\partial a_{r2}}{\partial x_{jp}} \\
k_3 &= \frac{C_d a_{r20} C_1}{\sqrt{T_0}} \\
k_4 &= \frac{C_{db} a_{lpp} C_1}{\sqrt{T_0}} \\
k_5 &= -\frac{C_{dm} a_{lpp} C_1}{\sqrt{T_0}} \\
k_6 &= \frac{1}{\rho_{10}} \\
k_7 &= \frac{1}{\rho_{20}}
\end{aligned}$$

$$\begin{aligned}
k_8 &= \frac{\gamma P_{10}}{V_{10}} \\
k_9 &= \frac{\gamma P_{20}}{V_{20}} \\
k_{10} &= k_6 k_8 (k_1 + k_4) \\
k_{11} &= k_5 k_6 k_8 \\
k_{12} &= k_4 k_7 k_9 \\
k_{13} &= k_7 k_9 (k_3 + k_5) \\
k_{14} &= k_0 k_6 k_8 \\
k_{15} &= k_2 k_7 k_9
\end{aligned}$$

References

1. **Aizerman, M.A.**, Ed., *Pneumatic and Hydraulic Control Systems*, Vol. 1 & 2, Pergamon Press, Oxford, England, 1968.

2. **Ali, M.S., Kyriakopoulos, K.J., Stephanou, H.E.**, "The kinematics of the Anthrobot-2 Dextrous Hand", in *Proc. IEEE International Conference on Robotics and Automation*, Atlanta, Georgia, pp. 705–710, May, 1993.

3. **Allen, P.K., Michelman, P., Roberts, K.S.**, "An integrated system for dextrous manipulation", in *Proc. IEEE International Conference on Robotics and Automation*, Scottsdale, Arizona, pp. 612–617, May, 1989.

4. **Allen, P.K., Roberts, K.S.**, "Haptic object recognition using a multi-fingered dextrous hand", in *Proc. IEEE International Conference on Robotics and Automation*, Scottsdale, Arizona, pp. 342–347, May, 1989.

5. **An, C.H., Atkeson, C.G., Hollerbach, J.M.**, *Model-Based Control of a Robot Manipulator*, MIT Press, Cambridge, Massachusetts, 1988.

6. **Andersen, B.W.**, *The Analysis and Design of Pneumatic Systems*, Robert E. Krieger Publishing Company, Malabar, Florida, 1976.

7. **Araki, K.**, "Frequency response of a pneumatic valve-controlled cylinder with an overlap four-way valve. Part I: Theoretical analysis", *Journal of Fluid Control*, Vol. 66, pp. 7–44, 1986.

8. **Araki, K.**, "Frequency response of a pneumatic valve-controlled cylinder with an overlap four-way valve. Part II: Experimental analysis", *Journal of Fluid Control*, Vol. 67, pp. 33–50, 1987.

9. **Bejczy, A.K., Salisbury, J.K.**, "Kinesthetic coupling between operator and remote manipulator", *Advances in Computer Technology, ASME*, Vol. 1, pp. 197–211, August, 1980.

10. **Bennett, D.J., Hollerbach, J.M.**, "Closed-loop kinematic calibration of the Utah-MIT Hand", in *Experimental Robotics I — The First International Symposium* (**Hayward, V., Khatib, O.**, Eds.), pp. 539–552, Springer-Verlag, 1990.

11. **Biggers, K.B., Jacobsen, S.C., Gerpheide, G.E.**, "Low-level control of the Utah/MIT Dextrous Hand", in *Proc. IEEE International Conference on Robotics and Automation*, San Francisco, California, pp. 61–66, April, 1986.

12. **Blackburn, J.F., Reethof, G., Shearer, J.L.**, *Fluid Power Control*, MIT Press, Cambridge, Massachusetts, 1960.

13. **Bobrow, J.E., Jabbari, F.**, "Adaptive pneumatic force actuation and position control", *Transactions of the ASME, Journal of Dynamic Systems, Measurement and Control*, Vol. 113, pp. 267–272, June, 1991.

14. **Botting, L.R., Eynon, G.T., Foster, K.**, "The response of a high-pressure pneumatic servomechanism to step and sinewave inputs", *Proc. Institution of Mechanical Engineers*, Vol. 184, No. 54, pp. 993–1012, 1969.

15. **Boulet, B., Daneshmend, L., Hayward, V., Nemri, C.**, "System identification and modelling of a high performance hydraulic actuator", in *Experimental Robotics 2 — The Second International Symposium* (**Chatila, R., Hirzinger, G.**, Eds.), Springer-Verlag, 1992.

16. **Bowns, D.E., Ballard, R.L.**, "Digital computation for the analysis of pneumatic actuator systems", *Proc. Institution of Mechanical Engineers*, Vol. 186, pp. 881–889, 1972.

17. **Burrows, C.R.**, "Effect of position on the stability of pneumatic servomechanisms", *Journal of Mechanical Engineering Science*, Vol. 11, No. 6, pp. 615–616, 1969.

18. **Burrows, C.R.**, *Fluid Power Servomechanisms*, van Nostrand Reinhold, London, England, 1972.

19. **Burrows, C.R., Webb, C.R.**, "Simulation of an on-off pneumatic servomechanism", *Proc. Institution of Mechanical Engineers*, Vol. 182, No. 29, pp. 631–642, 1967.

20. **Chen, F.Y.**, "Dynamic response of a cam-actuated mechanism with pneumatic coupling", *Transactions of the ASME, Journal of Engineering for Industry*, Vol. 99, No. 3, pp. 598-603, 1977.

21. **Craig, J.J.**, *Introduction to Robotics: Mechanics and Control*, Second ed., Addison-Wesley, Reading, Massachusetts, 1989.

22. **de Pennington, A., 't Mannetje, J.J., Bell, R.**, "The modelling of electrohydraulic control valves and its influence on the design of electrohydraulic drives", *Journal of Mechanical Engineering Science*, Vol. 16, No. 3, pp. 196–204, 1974.

23. **Fantuzzi, C., Rossi, C., Tonielli, A., Vassura, G.**, "A smart sensory and actuation system for the University of Bologna Robotic Hand: Latest developments and implementations", in *Proc. Second International Symposium on Measurement and Control in Robotics*, Tsukuba Science City, Japan, pp. 515–522, November, 1992.

24. **Farry, K.A., Walker, I.D.**, "Myoelectric teleoperation of a complex robotic hand", in *Proc. IEEE International Conference on Robotics and Automation*, Atlanta, Georgia, pp. 502-509, May, 1993.

25. **Frame, J.G., Mohan, N., Liu, T.**, "Hysteresis modeling in an electromagnetic transients program", *IEEE Transactions on Power Apparatus and Systems*, Vol. PAS-101, No. 9, pp. 3403–3411, September, 1982.

26. **Funakubo, H.**, Ed., *Actuators for Control*, Vol. 2 of Precision Machinery and Robotics, Gordon and Breach Science Publishers, New York, New York, 1991.

27. **Grupen, R.**, "Planning grasp strategies for multifingered robot hands", in *Proc. IEEE International Conference on Robotics and Automation*, Sacramento, California, pp. 646–651, April, 1991.

28. **Guo, G., Gruver, W.A., Qian, X.**, "A new design for a dextrous robotic hand mechanism", *IEEE Control Systems Magazine*, pp. 35–38, August, 1992.

29. **Handroos, H.M., Vilenius, M.J.**, "The utilization of experimental data in modelling hydraulic single stage pressure control valves", *Transactions of the ASME, Journal of Dynamic Systems, Measurement and Control*, Vol. 112, pp. 482–488, September, 1990.

30. **Hashimoto, H., Ogawa, H., Obama, M., Umeda, T., Tatuno, K., Furukawa, T.**, "Development of a multi-fingered robot hand with fingertip tactile sensors", in *Proc. IEEE/RSJ International Conference on Intelligent Robots and Systems*, Yokohama, Japan, pp. 875–882, July, 1993.

31. **Henri, P.D., Hollerbach, J.M.**, "An analytical and experimental investigation of a jet pipe controlled electropneumatic actuator", in *Proc. IEEE International Conference on Robotics and Automation*, San Diego, California, May, 1994. (In press).

32. **Hollerbach, J.M., Hunter, I.W., Ballantyne, J.**, "A comparative analysis of actuator technologies for robotics", in *The Robotics Review 2* (**Khatib, O., Craig, J.J., Lozano-Perez, T.**, Eds.), pp. 299–342, MIT Press, Cambridge, Massachusetts, 1992.

33. **Hong, J., Tan, X.**, "Calibrating a VPL DataGlove for teleoperating the Utah/MIT Hand", in *Proc. IEEE International Conference on Robotics and Automation*, Scottsdale, Arizona, pp. 1752–1757, May, 1989.

34. **Hunter, I.W., Lafontaine, S., Hollerbach, J.M., Hunter, P.J.**, "Fast reversible NiTi fibers for use in microrobotics", in *Proc. IEEE Workshop on Micro Electro Mechanical Systems*, Nara, Japan, pp. 166–170, January, 1991.

35. **Jacobsen, S.C., Iversen, E.K., Davis, C.C., Potter, D.M., McLain, T.W.**, "Design of a multiple degree of freedom. force reflective hand master/slave with a high mobility wrist", in *Proc. Third Topical Meeting on Robotics and Remote Systems*, Charleston, South Carolina, March, 1989a.

36. **Jacobsen, S.C., Iversen, E.K., Knutti, D.F., Johnson, R.T., Biggers, K.B.**, "Design of the Utah/MIT Dextrous Hand", in *Proc. IEEE International Conference on Robotics and Automation*, San Francisco, California, pp. 1520–1534, April, 1986.

37. **Jacobsen, S.C., Knutti, D.F., Biggers, K.B., Iversen, E.K., Wood, J.E.**, "An electropneumatic actuation system for the Utah/MIT Dextrous Hand", in *Theory and Practice of Robots and Manipulators. Proc. RoManSy '84: The Fifth CISM/IFToMM Symposium*, Udine, Italy, pp. 271–279, June, 1984a.

38. **Jacobsen, S.C., Ko, H., Iversen, E.K., Davis, C.C.**, "Antagonistic control of a tendon driven manipulator", in *Proc. IEEE International Conference on Robotics and Automation*, Scottsdale, Arizona, pp. 1334–1339, May, 1989b.

39. **Jacobsen, S.C., Ko, H., Iversen, E.K., Davis, C.C.**, "Control strategies for tendon-driven manipulators", *IEEE Control Systems Magazine*, Vol. 10, pp. 23–28, February, 1990.

40. **Jacobsen, S.C., McCammon, I.D., Biggers, K.B., Phillips, R.P.**, "Design of tactile sensing systems for dextrous manipulators", *IEEE Control Systems Magazine*, Vol. 8, pp. 3–13, February, 1988.

41. **Jacobsen, S.C, Wood, J.E., Knutti, D.F., Biggers, K.B.**, "The Utah/MIT Dextrous Hand: Work in progress", *International Journal of Robotics Research*, Vol. 3, No. 4, pp. 21–50, 1984b.

42. **Jacobsen, S.C., Wood, J.E., Knutti, D.F., Biggers, K.B., Iversen, E.K.**, "The Version I Utah/MIT Dextrous Hand", in *Robotics Research: The Second International Symposium* (**Hanafusa, H., Inoue, H.**, Eds.), pp. 301 308, MIT Press, 1984c.

43. **Jau, B.M.**, "Man-equivalent telepresence through four fingered human-like hand system", in *Proc. IEEE International Conference on Robotics and Automation*, Nice, France, pp. 843–848, May, 1992.

44. **Johnstun, C.R., Smith, C.C.**, "Modeling and design of a mechanical tendon actuation system", *Transactions of the ASME, Journal of Dynamic Systems, Measurement and Control*, Vol. 114, pp. 253-261, June, 1992.

45. **Kaneko, M., Paetsch, W., Tolle, H.**, "Input-dependent stability of joint torque control of tendon-driven robot hands", *IEEE Transactions on Industrial Electronics*, Vol. 39, No. 2, pp. 96-103, April, 1992.

46. **Kaneko, M., Wada, M., Maekawa, H., Tanie, K.**, "A new consideration on tendon-tension control system of robot hands", in *Proc. IEEE International Conference on Robotics and Automation*, Sacramento, California, pp. 1028 1033, April, 1991.

47. **Kawakami, Y., Akao, J., Kawai, S.**, "Some considerations on the dynamic characteristics of pneumatic cylinders", *Journal of Fluid Control*, Vol. 75, pp. 22–36, 1988.

48. **Ko, H., Davis, C.C., Iversen, E.K., Jacobsen, S.C.**, "High stiffness and low slew drag in an antagonistic control system", in *Proc. IEEE International Conference on Robotics and Automation*, Cincinnati, Ohio, pp. 1879–1884, May, 1990.

49. **Kunt, C., Singh, R.**, "A linear time varying model for on-off valve controlled pneumatic actuators", *Transactions of the ASME, Journal of Dynamic Systems, Measurement and Control*, Vol. 112, pp. 740–747, December, 1990.

50. **Kunt, C., Singh, R.**, "Application of Floquet theory to on-off valve controlled pneumatic actuators", *Transactions of the ASME, Journal of Dynamic Systems, Measurement and Control*, Vol. 114, pp. 299–305, June, 1992.

51. **Kuribayashi, K.**, "A new compact robot hand using TiNi alloy actuator and stepping motor controlled by micro-computer", in *IECON '86*, pp. 538–543, 1986.

52. **Lai, J., Menq, C., Singh, R.**, "Accurate position control of a pneumatic actuator", *Transactions of the ASME, Journal of Dynamic Systems, Measurement and Control*, Vol. 112, pp. 734–739, December, 1990.

53. **Liu, S., Bobrow, J.E.**, "An analysis of a pneumatic servo system and its application to a computer-controlled robot", *Transactions of the ASME, Journal of Dynamic Systems, Measurement and Control*, Vol. 110, pp. 228–235, September, 1988.

54. **Loucks, C.S., Johnson, V.J., Boissiere, P.T., Starr, G.P., Steele, J.P.H.**, "Modeling and control of the Stanford/JPL Hand", in *Proc. IEEE International Conference on Robotics and Automation*, Raleigh, North Carolina, pp. 573–578, April, 1987.

55. **Maekawa, H., Yokoi, K., Tanie, K., Kaneko, M., Kimura, N., Imamura, N.**, "Development of a three-fingered robot hand with stiffness control capability", *Mechatronics*, Vol. 2, No. 5, pp. 483–494, 1992.

56. **Martin, D.J., Burrows, C.R.**, "The dynamic characteristics of an electrohydraulic servovalve", *Transactions of the ASME, Journal of Dynamic Systems, Measurement and Control*, Vol. 98, pp. 395–406, December, 1976.

57. **McLain, T.W., Iversen, E.K., Davis, C.C., Jacobsen, S.C.**, "Development, simulation and validation of a highly nonlinear hydraulic servosystem model", in *Proc. 1989 American Control Conference, AACC*, Pittsburgh, Pennsylvania, pp. 385–391, June, 1989.

58. **Michelman, P., Allen, P.**, "Compliant manipulation with a dextrous robot hand", in *Proc. IEEE International Conference on Robotics and Automation*, Atlanta, Georgia, pp. 711–716, May, 1993.

59. **Nahvi, A., Hollerbach, J.M., Xu, Y., Hunter, I.W.**. "An investigation of the transmission system of a tendon driven robot hand", in *Proc. IEEE/RSJ International Conference on Intelligent Robots and Systems*, Munich, Germany, September, 1994. (In press).

60. **Nakano, Y., Fujie, M., Hosada, Y.**, "Hitachi's robot hand", *Robotics Age*, Vol. 6, No. 7, pp. 18–20, 1984.

61. **Narasimhan, S.**, *Dextrous Robotic Hands: Kinematics and Control*, Master's Thesis, Department of Electrical Engineering and Computer Science, Massachusetts Institute of Technology, January, 1988.

62. **Narasimhan, S., Siegel, D.M.**, "The CONDOR programmer's manual — Version II", Artificial Intelligence Laboratory, Massachusetts Institute of Technology, July, 1987.

63. **Narasimhan, S., Siegel, D.M., Hollerbach, J.M.**, "Condor: A revised architecture for controlling the Utah-MIT hand", in *Proc. IEEE International Conference on Robotics and Automation*, Philadelphia, Pennsylvania, pp. 446–449, April, 1988.

64. **Narasimhan, S., Siegel, D.M., Hollerbach, J.M.**, "CONDOR: An architecture for controlling the Utah/MIT Dextrous Hand", *IEEE Transactions on Robotics and Automation*, Vol. 5, No. 5, pp. 616 627, October, 1989.

65. **Narasimhan, S., Siegel, D., Hollerbach, J.M., Biggers, K., Gerpheide, G.**, "Implementation of control methodologies on the computational architecture for the Utah/MIT Hand", in *Proc. IEEE International Conference on Robotics and Automation*, San Francisco, California, pp. 1884–1889, April, 1986.

66. **Noritsugu, T.**, "Development of PWM mode electro-pneumatic servomechanism. Part I: Speed control of a pneumatic cylinder", *Journal of Fluid Control*, Vol. 66, pp. 65–80, 1986.

67. **Noritsugu, T.**, "Development of PWM mode electro-pneumatic servomechanism. Part II: Position control of a pneumatic cylinder", *Journal of Fluid Control*, Vol. 67, pp. 7–32, 1987.

68. **Okada, T.**, "Object-handling system for manual industry", *IEEE Transactions on Systems, Man and Cybernetics*, Vol. SMC-9, No. 2, pp. 79- 89, February, 1979.

69. **Pao, L., Speeter, T.H.**, "Transformation of human hand positions for robotic hand control", in *Proc. IEEE International Conference on Robotics and Automation*, Scottsdale, Arizona, pp. 1758--1763, May, 1989.

70. **Perlin, K., Demmel, J.W., Wright, P.K.**, "Simulation software for the Utah/MIT Dextrous Hand", *Robotics and Computer-Integrated Manufacturing*, Vol. 5, No. 4, pp. 281–292, 1989.

71. **Press, W.H., Teukolsky, S.A., Vetterling, W.T., Flannery, B.P.**, *Numerical Recipes in C*, Second ed., Cambridge University Press, Cambridge, England, 1992.

72. **Rockenbeck, W.H.**, "Static load estimation using the Utah/MIT Dextrous Hand", Bachelor's Thesis, Department of Electrical Engineering and Computer Science, Massachusetts Institute of Technology, May, 1989.

73. **Rohling, R.N., Hollerbach, J.M.**, "Optimized fingertip mapping for teleoperation of dextrous robot hands", in *Proc. IEEE International Conference on Robotics and Automation*, Atlanta, Georgia, pp. 769–775, May, 1993.

74. **Rohling, R.N., Hollerbach, J.M.**, "Modeling and parameter estimation of the human index finger", in *Proc. IEEE International Conference on Robotics and Automation*, San Diego, California. May, 1994. (In press).

75. **Rohling, R.N., Hollerbach, J.M., Jacobsen, S.C.**, "Optimized fingertip mapping: A general algorithm for robotic hand teleoperation". *Presence: Teleoperators and Virtual Environments*. 1994. (In press).

76. **Salisbury, J.K., Craig, J.J.**, "Articulated hands: Force control and kinematic issues", *International Journal of Robotics Research*. Vol. 3, No. 4, pp. 4–17, 1982.

77. **Sarcos Research Corporation**, "Sarcos MicroServoSystems: Integrated linear pneumatic actuators". Product literature.

78. **Shapiro, A.H.**, *The Dynamics and Thermodynamics of Compressible Fluid Flow*, Vol. 1, Ronald Press, New York, New York, 1953.

79. **Shearer, J.L.**, "Study of pneumatic processes in the continuous control of motion with compressed air — I & II", *Transactions of the ASME*, Vol. 78, pp. 233–249, February, 1956.

80. **Shearer, J.L.**, "Nonlinear analog study of a high-pressure pneumatic servomechanism", *Transactions of the ASME*, Vol. 79, pp. 465–472, 1957.

81. **Shearer, J.L.**, "The effects of radial clearance, rounded corners, and underlap on servovalve characteristics", in *Proc. Joint Automatic Control Conference*, 1980.

82. **Siegel, D.M., Narasimhan, S., Hollerbach, J.M., Gerpheide, G.E, Kriegman, D.J.**, "Computational architecture for the Utah/MIT Hand", in *Proc. IEEE International Conference on Robotics and Automation*, St. Louis, Missouri, pp. 918–925, March, 1985.

83. **Speeter, T.H.**, "Primitive based control of the Utah/MIT Dextrous Hand", in *Proc. IEEE International Conference on Robotics and Automation*, Sacramento, California, pp. 866-877, April, 1991.

84. **Speeter, T.H.**, "Transforming human hand motion for telemanipulation", *Presence: Teleoperators and Virtual Environments*, Vol. 1, No. 1, pp. 63 79, Winter, 1992.

85. **'t Mannetje, J.J.**, "Pneumatic servo design method improves system bandwidth twenty-fold", *Control Engineering*, Vol. 28, No. 6, pp. 79 83, June, 1981.

86. **Taft, C.K., Harned, T.J.**, "Low power electro-pneumatic control valve", in *Proc. Joint Automatic Control Conference*, 1980.

87. **Talukdar, S.N., Bailey, J.R.**, "Hysteresis models for system studies", *IEEE Transactions on Power Apparatus and Systems*, Vol. PAS-95, No. 4, pp. 1429 1434, July/August, 1976.

88. **Thayer, W.J.**, "Specification standards for electrohydraulic flow control servovalves", Technical Bulletin 117, Moog Inc., East Aurora, New York, 1962.

89. **Thayer, W.J.**, "Electropneumatic servoactuation: An alternative to hydraulics for some low power applications", Technical Bulletin 151, Moog Inc., East Aurora, New York, 1984.

90. **Threlfall, D.C.**, "The inclusion of Coulomb friction in mechanisms programs with particular reference to DRAM", *Mechanism and Machine Theory*, Vol. 13, pp. 475–483, 1978.

91. **Townsend, W.T.**, "The effect of transmission design on force-controlled manipulator performance", Tech. Rep. 1054, MIT Artificial Intelligence Laboratory, April, 1988.

92. **Townsend, W.T., Salisbury, J.K.**, "The efficiency limit of belt and cable drives", *Transactions of the ASME, Journal of Mechanisms, Transmissions and Automation in Design*, Vol. 110, pp. 303–307, September, 1988.

93. **Townsend, W.T., Salisbury, J.K.**, "Mechanical bandwidth as a guideline to high-performance manipulator design", in *Proc. IEEE International Conference on Robotics and Automation*, Scottsdale, Arizona, pp. 1390–1395, May, 1989.

94. **Venkataraman, S.T., Iberall, T.**, *Dextrous Robot Hands*, Springer-Verlag, New York, New York, 1990.

95. **Wang, Y.T., Singh, R.**, "Pneumatic chamber nonlinearities". *Transactions of the ASME, Journal of Applied Mechanics*, Vol. 53, pp. 956–958, December, 1986.

96. **Xu, Y., Hollerbach, J.M., Ma, D.**, "Force and contact transient control using nonlinear PD control", in *Proc. IEEE International Conference on Robotics and Automation*, San Diego, California, May, 1994. (In press).

97. **Xu, Y., Ma, D., Hollerbach, J.M.**, "Nonlinear proportional and derivative control for high disturbance rejection and high gain force control", in *Proc. IEEE International Conference on Robotics and Automation*, Atlanta, Georgia, pp. 752–759, May, 1993.